

Naval Research Laboratory

Washington, DC 20375-5320



AD-A255 414



NRL/MR/4795-92-7114

Beam Trapping in a Modified Betatron With a Localized Bipolar Electric Field Pulse

J. MATHEW AND C. A. KAPETANAKOS

*Beam Physics Branch
Plasma Physics Division*

S. J. MARSH

*SFA Inc.
Landover, MD 20785*

AND

D. DIALETIS

*SAIC
McLean, VA 22102*

August 24, 1992



92-25272

Supported by SPAWAR and the Office of Naval Research

92 9 15 050

Approved for public release; distribution is unlimited.

Public reporting burden for this collection of information is estimated to average 1 hour per response, including the time for reviewing instructions, searching existing data sources, gathering and maintaining the data needed, and completing and reviewing the collection of information. Send comments regarding this burden estimate or any other aspect of this collection of information, including suggestions for reducing this burden, to Washington Headquarters Services, Directorate for Information Operations and Reports, 1215 Jefferson Davis Highway, Suite 1204, Arlington, VA 22202-4302, and to the Office of Management and Budget, Paperwork Reduction Project (0704-0188), Washington, DC 20503.

1. AGENCY USE ONLY (Leave Blank)		2. REPORT DATE August 24, 1992		3. REPORT TYPE AND DATES COVERED Interim	
4. TITLE AND SUBTITLE Beam Trapping in a Modified Betatron With a Localized Bipolar Electric Field Pulse				5. FUNDING NUMBERS	
6. AUTHOR(S) J. Mathew, S. J. Marsh, ¹ D. Dialetis, ² and C. A. Kapetanakis					
7. PERFORMING ORGANIZATION NAME(S) and ADDRESS(ES) Naval Research Laboratory Washington, DC 20375-5320				8. PERFORMING ORGANIZATION REPORT NUMBER NRL/FR-4795-92-7114	
9. SPONSORING/MONITORING AGENCY NAME(S) AND ADDRESS(ES) SPAWAR Washington, DC 20363 ONR Arlington, VA 22217				10. SPONSORING/MONITORING AGENCY REPORT NUMBER	
11. SUPPLEMENTARY NOTES ¹ SFA Inc., Landover, MD 20785 ² SAIC, McLean, VA 22102					
12a. DISTRIBUTION/AVAILABILITY STATEMENT Approved for public release; distribution is unlimited.				12b. DISTRIBUTION CODE	
13. ABSTRACT (Maximum 200 words) This paper describes a scheme for trapping the injected beam in a modified betatron accelerator using a localized inductive electric field pulse generated by a charged coaxial pulseline. The average canonical angular momentum $\langle P_\theta \rangle$ is not conserved in this scheme. Numerical simulations demonstrate trapping over a wide range of operating parameters. A 0.84-Ω, 45-ns water dielectric pulseline has been built for testing the trapping concept. The pulseline is switched using triggered vacuum surface flashover switches. By crowbarring the pulseline, its output is limited to a single bipolar pulse that has a ~22 ns rise time.					
14. SUBJECT TERMS Modified betatron Beam trapping Toroidal pulseline				15. NUMBER OF PAGES 52	
				16. PRICE CODE	
17. SECURITY CLASSIFICATION OF REPORT UNCLASSIFIED	18. SECURITY CLASSIFICATION OF THIS PAGE UNCLASSIFIED	19. SECURITY CLASSIFICATION OF ABSTRACT UNCLASSIFIED	20. LIMITATION OF ABSTRACT SAR		

CONTENTS

I. INTRODUCTION	1
II. THE ELECTRIC FIELD PULSE	2
III. WAVE PROPAGATION IN TOROIDAL GEOMETRY	6
IV. NUMERICAL RESULTS	15
V. PULSELINE CONSTRUCTION	17
VI. EXPERIMENTAL RESULTS	21
VII. DISCUSSION	26
VIII. SUMMARY AND CONCLUSIONS	29
REFERENCES	30
DISTRIBUTION LIST	49

DTIC QUALITY INSPECTED 3

Accession For	
NTIS GRA&I	<input checked="" type="checkbox"/>
DTIC TAB	<input type="checkbox"/>
Unannounced	<input type="checkbox"/>
Justification	
By _____	
Distribution/	
Availability Codes	
Dist	Avail and/or Special
A-1	

BEAM TRAPPING IN A MODIFIED BETATRON WITH A LOCALIZED BIPOLAR ELECTRIC FIELD PULSE

I. INTRODUCTION

Compact, high-current accelerators are currently under development in several laboratories.¹⁻⁵ Among these accelerators is the modified betatron.⁶⁻⁸ This accelerator is a toroidal, closed orbit device that utilizes three different magnetic fields to accelerate and confine the high current electron ring; the time varying betatron or vertical field that controls mainly the major radius of the electron ring and also is responsible for the acceleration, the quasi-static toroidal magnetic field that controls primarily the minor radius of the ring and also the growth rate of the various unstable modes and finally the quasi-static strong focusing (SF) field that reduces the sensitivity of the electron orbits to energy mismatch and spread.

A challenging physics issue of the modified betatron concept is the capture of the injected beam into the closed magnetic field configuration of the device. Capture of the beam requires that its poloidal orbit be modified within a bounce period τ_B , i.e., within a poloidal revolution around the equilibrium position. Modification of the beam's poloidal orbit can be achieved by either changing the equilibrium position of the gyrating electrons or by reducing the radius of the poloidal orbit.

The strong focusing field in the modified betatron is generated by a set of stellarator windings. Since this field is a function of the toroidal angle, the canonical angular momentum P_θ is not conserved. However, when P_θ is averaged over the intermediate frequency mode of the system ω_w ($= 4\pi v_\theta / L_{sf}$, where v_θ is the toroidal velocity and L_{sf} is the period of the SF windings), the averaged $\langle P_\theta \rangle$ is an approximate constant of the motion.¹⁰ Two different schemes¹⁰⁻¹² have been developed, so far, for trapping the beam

in the modified betatron. In both schemes $\langle P_\theta \rangle$ is an approximate invariant. In this paper, we discuss an additional trapping approach, in which $\langle P_\theta \rangle$ is not conserved. The proposed trapping scheme is based on the change of the centroid's equilibrium position by a localized electric field. This electric field pulse is produced by a coaxial pulseline and has a pulsewidth comparable to the bounce period of the beam.

This paper is organized as follows: Section II briefly reviews the generation of the localized electric field pulse. Section III treats the propagation of electromagnetic waves in toroidal geometry. Beam centroid orbits from the numerical integration of equations of motion are presented in Section IV. Section V describes the constructional details of the pulseline and the experimental data are presented in Section VI. An interesting feature observed in the experiment is discussed in Section VII, and Section VIII contains a brief summary of the results and some important conclusions.

II. THE ELECTRIC FIELD PULSE

Although the pulseline that is described in Section V is toroidal, the discussion in this Section is limited for simplicity to the coaxial, cylindrical pulseline shown in Fig. 1. This pulseline is similar to the radial line initially employed by Pavlovskii *et al.*,¹³ and analyzed by Eccleshall and Temperley.¹⁴ In this Section, we briefly review the pulseline for completeness.

The voltage at the gap V_g of the pulseline after the switch closes can be found by integrating the equation $\nabla \times \vec{E} = -\partial \vec{B} / \partial t$ along the dash line of Fig. 1. Assuming that the resistivity of the conductor can be neglected, then

$$V_o = \oint \vec{E} \cdot d\vec{\ell} = -\frac{\partial \Phi}{\partial t}, \quad (1)$$

where Φ is the magnetic flux through the area A surrounded by the dash line.

The magnetic field of the propagating wave is found by integrating the equation $\nabla \times \vec{B} = \mu \vec{j} + \mu \epsilon (\partial \vec{E} / \partial t)$ in the circular area D that is located just behind the wave front.

The result is

$$B = -\mu I_\ell / 2\pi R, \quad (2)$$

where I_ℓ is the current of the line, and R is the radius of the circular area.

The magnetic flux Φ can be computed from

$$\Phi = \int_A \vec{B} \cdot d\vec{S}, \quad (3)$$

where B is given by Eq. (2). Substituting (2) into (3), we obtain

$$\Phi = \begin{cases} -\frac{\mu I_\ell U t}{2\pi} \ln \left(\frac{R_3}{R_2} \right), & \text{for } t \leq \tau \\ -\frac{\mu I_\ell U}{2\pi} \ln \left(\frac{R_3}{R_2} \right) (2\tau - t), & \text{for } \tau \leq t \leq 3\tau, \end{cases} \quad (4)$$

where U is the speed of the electromagnetic wave, $\tau = 2\ell/U$ is the one-way transit time, ℓ is the length of the pulseline (see Fig. 1), and it has been assumed that $R_2 = \sqrt{R_3 R_1}$.

Since the characteristic impedance Z_o of the line is given by

$$Z_o = \frac{1}{2\pi} \sqrt{\frac{\mu}{\epsilon}} \ln \left(\frac{R_3}{R_2} \right), \quad (5)$$

and $V_o = I_\ell Z_o$, where V_o is the initial voltage of the line, Eqs. (1) and (4) give

$$V_g = \begin{cases} V_o, & \text{for } t \leq \tau \\ -V_o, & \text{for } \tau \leq t \leq 3\tau. \end{cases}$$

Up to this point the effect of the beam (load) has been neglected. The beam induces a voltage V_b at the gap and thus the accelerating voltage is reduced, i.e.,

$$V_g = V_o - V_b. \quad (6)$$

Since $V_b = I_b Z_o$, where I_b is the beam current and assuming that the beam is matched to the line, i.e., $V_g = I_b Z_o$, Eq. (6) gives $V_g = V_o/2$. When the beam is matched to the line all the energy that is initially stored in the line is transferred to the beam and thus the efficiency of the system is 100%.

If ΔE is the beam energy change required to move the beam equilibrium position by a few centimeters, and τ_o is the period of revolution around the major axis, then

$$\Delta E = \left(\frac{V_o}{2} \right) \frac{2\tau}{\tau_o}, \quad (7)$$

for the case where the injected beam interacts with the pulseline during the period $\tau \leq t \leq 3\tau$.

Since $I_b = V_o/2Z_o$, Eq. (7) together with the expressions for τ and Z_o given previously, yield

$$\ell \ln \frac{R_3}{R_2} = \frac{\Delta E \tau_o \pi}{2\mu I_b}. \quad (8)$$

In the NRL modified betatron the ratio R_3/R_2 is restricted to values close to unity by the presence of the strong focusing windings. Therefore, the length of the line is unac-

ceptably large. This difficulty can be avoided by mismatching the beam. In this case, the initial voltage of the line is made larger than the value needed for matching, namely $2I_b Z_o$. Then the voltage at the gap is $V_g = V_o - I_b Z_o$, and the length of the line is given by

$$\ell = \frac{\Delta E \tau_o c}{4\sqrt{\epsilon/\epsilon_o} [V_o - I_b Z_o]}. \quad (9)$$

For $\Delta E = 60$ keV, $\tau_o = 24$ ns, $\epsilon/\epsilon_o = 80$, $V_o = 20$ kV, $I_b = 2$ kA, $R_1 = 16.8$ cm, $R_2 = 19.0$ cm and $R_3 = 21.6$ cm, $Z_o = 0.84 \Omega$ and Eq. (9) gives $\ell = 0.66$ m. Although lower than in the case of the matched beam, the system efficiency is still resonable and is given by

$$\epsilon_f = \frac{4Z_o I_b}{V_o^2} (V_o - I_b Z_o). \quad (10)$$

For the parameters listed above $\epsilon_f \simeq 31\%$.

Plots of Z_o , ℓ , ϵ_f , and τ as a function of ϵ/ϵ_o for the parameters given above are shown in Fig. 2. For a matched beam, Eq. (10) gives an efficiency of 100%, and at time $t = 3\tau$ there is no energy left in the pulseline. The interaction of a beam with a charged pulseline cavity can be better understood using superposition. It can be shown that the gap voltage is the sum of the open circuit voltage at the gap of the charged pulseline in the absence of the beam, and the gap voltage induced by the beam in the absence of any charge voltage. If the beam is present beyond $t = 3\tau$ (as is the case with a cyclic accelerator like the modified betatron), energy will be transferred from the beam back to the pulseline during the period $3\tau \leq t \leq 5\tau$. This is the case regardless of whether the beam is matched to the pulseline or not. Fig. 3 shows the gap voltage for a matched beam injected at $t = \tau$.

To avoid beam interactions beyond $t = 3\tau$, the pulseline needs to be crowbarred by firing a set of switches located in the insulating gap region. This isolates the pulseline from the circulating electron beam. Pulselines used in linear accelerators do not need crowbar switches because the beam duration is usually less than 2τ .

III. WAVE PROPAGATION IN TOROIDAL GEOMETRY

Let (r, θ, z) be the cylindrical coordinates and $\vec{e}_r, \vec{e}_\theta, \vec{e}_z$ be the unit vectors in cylindrical geometry. Then the electromagnetic field can be decomposed into its toroidal components E_θ, B_θ and its transverse components \vec{E}_t, \vec{B}_t , namely:

$$\vec{E} = \vec{E}_t + E_\theta \vec{e}_\theta, \quad (11a)$$

$$\vec{B} = \vec{B}_t + B_\theta \vec{e}_\theta, \quad (11b)$$

where

$$\vec{E}_t = E_r \vec{e}_r + E_z \vec{e}_z, \quad (12a)$$

$$\vec{B}_t = B_r \vec{e}_r + B_z \vec{e}_z, \quad (12b)$$

It is assumed that the electromagnetic field can be expressed in the form

$$\vec{E} = \vec{E}(r, z) e^{-i\omega t + im\theta}, \quad (13a)$$

$$\vec{B} = \vec{B}(r, z) e^{-i\omega t + im\theta}, \quad (13b)$$

where ω is the frequency and m is an integer ($m \neq 0$). Then, it is possible to show from Maxwell's equations (in MKS units) that the transverse components can be expressed in terms of the toroidal components as follows:

$$\vec{E}_t = \frac{1}{k^2 - (m/r)^2} \left[\frac{im}{r} \nabla_t E_\theta - i\omega \vec{e}_\theta \times \nabla_t B_\theta + \frac{im}{r^2} E_\theta \vec{e}_r + i\omega \frac{1}{r} B_\theta \vec{e}_z \right], \quad (14a)$$

$$\tilde{B}_t = \frac{1}{k^2 - (m/r)^2} \left[\frac{im}{r} \nabla_t B_\theta + \frac{ik^2}{\omega} \tilde{e}_\theta \times \nabla_t E_\theta + \frac{im}{r^2} B_\theta \tilde{e}_r - \frac{ik^2}{\omega} \frac{1}{r} E_\theta \tilde{e}_z \right], \quad (14b)$$

where

$$\nabla_t = \tilde{e}_r \frac{\partial}{\partial r} + \tilde{e}_z \frac{\partial}{\partial z}, \quad (15)$$

$k = \sqrt{\mu_r \epsilon_r}(\omega/c)$, μ_r and ϵ_r are the relative permeability and relative permittivity of the medium, and c is velocity of light in vacuum.

After a lengthy computation, it can be shown that the toroidal components satisfy the following coupled set of differential equations:

$$\begin{aligned} \left(\frac{1}{r} \frac{\partial}{\partial r} r \frac{\partial}{\partial r} + \frac{\partial^2}{\partial z^2} \right) E_\theta - \frac{2m^2}{k^2 - (m/r)^2} \frac{1}{r^3} \frac{\partial E_\theta}{\partial r} + \left[k^2 - \frac{m^2 + 1}{r^2} - \frac{2m^2}{k^2 - (m/r)^2} \frac{1}{r^4} \right] E_\theta \\ + \frac{2m\omega}{k^2 - (m/r)^2} \frac{1}{r^2} \frac{\partial B_\theta}{\partial z} = 0, \end{aligned} \quad (16a)$$

$$\begin{aligned} \left(\frac{1}{r} \frac{\partial}{\partial r} r \frac{\partial}{\partial r} + \frac{\partial^2}{\partial z^2} \right) B_\theta - \frac{2m^2}{k^2 - (m/r)^2} \frac{1}{r^3} \frac{\partial B_\theta}{\partial r} + \left[k^2 - \frac{m^2 + 1}{r^2} - \frac{2m^2}{k^2 - (m/r)^2} \frac{1}{r^4} \right] B_\theta \\ - \frac{2m(k^2/\omega)}{k^2 - (m/r)^2} \frac{1}{r^2} \frac{\partial E_\theta}{\partial z} = 0. \end{aligned} \quad (16b)$$

These equations indicate that it is not possible to have pure TE or TM modes in a toroidal cavity. But it is possible to have solutions with a small E_θ or B_θ component, inversely proportional to r . In the first case, the solutions determine the pseudo-TE modes

and in the second case, the pseudo-TM modes. Notice that when Eqs. (16a) and (16b) are solved, the transverse components can be computed from Eqs. (14a) and (14b).

In order to solve Eqs. (16a) and (16b), we shall make use of the following theorem:

Let G_m and H_m be the solutions of the differential equation

$$\left(\frac{1}{r} \frac{\partial}{\partial r} r \frac{\partial}{\partial r} + \frac{\partial^2}{\partial z^2} \right) F_m + \left[k^2 - \frac{m^2}{r^2} \right] F_m = 0. \quad (17)$$

Then the set of toroidal components

$$E_\theta = \frac{\partial}{\partial z} [G_{m-1}(r, z) + H_{m+1}(r, z)] e^{-i\omega t + im\theta}, \quad (18a)$$

$$B_\theta = \frac{1}{\omega} \left[\left(k^2 - \frac{m^2}{r^2} \right) (G_{m-1}(r, z) - H_{m+1}(r, z)) + \frac{m}{r} \left(\frac{\partial}{\partial r} + \frac{1}{r} \right) (G_{m-1}(r, z) + H_{m+1}(r, z)) \right] e^{-i\omega t + im\theta}, \quad (18b)$$

satisfies the differential equations (16a) and (16b). The same is true for the set

$$B_\theta = \frac{\partial}{\partial z} [G_{m-1}(r, z) + H_{m+1}(r, z)] e^{-i\omega t + im\theta}, \quad (19a)$$

$$E_\theta = -\frac{\omega}{k^2} \left[\left(k^2 - \frac{m^2}{r^2} \right) (G_{m-1}(r, z) - H_{m+1}(r, z)) + \frac{m}{r} \left(\frac{\partial}{\partial r} + \frac{1}{r} \right) (G_{m-1}(r, z) + H_{m+1}(r, z)) \right] e^{-i\omega t + im\theta}, \quad (19b)$$

The first set (Eq. (18)) is appropriate for the computation of the pseudo-TE modes and the second set (Eq. (19)) is appropriate for the pseudo-TM modes, although both modes can be derived from either set.

All the results given above are valid for any toroidal cavity. In the following we shall confine ourselves to a toroidal conductor with rectangular cross section. Figure 4 illustrates the geometry of the problem. The inner and outer surfaces of the conductor are at $r = a$ and $r = b$, while the lower and upper surfaces lie at $z = 0$ and $z = D$. By direct inspection of Maxwell's equations it is easy to show that for such a toroidal conductor the boundary conditions are:

$$E_\theta = 0, \quad (20a)$$

$$\frac{\partial}{\partial r} r B_\theta = 0 \quad (20b)$$

at $r = a$ and $r = b$, and

$$E_\theta = 0, \quad (21a)$$

$$\frac{\partial B_\theta}{\partial z} = 0, \quad (21b)$$

at $z = 0$ and $z = D$. For a rectangular toroidal conductor, the solution of Eq. (7) is separable. First, let us consider the pseudo-TE modes. A solution of Eq. (17) is

$$G_m(r, z) = \frac{1}{2} (A J_m(\beta r) + B Y_m(\beta r)) \cos \frac{q\pi z}{D}, \quad (22)$$

where $J_m(x)$, $Y_m(x)$ are the Bessel functions of the first and second kind, and

$$\beta^2 = k^2 - \left(\frac{q\pi}{D}\right)^2 = \mu_r \epsilon_r \left(\frac{\omega}{c}\right)^2 - \left(\frac{q\pi}{D}\right)^2 \quad (23)$$

Let us also choose $H_m(r, z) = G_m(r, z)$. Then,

$$G_{m-1} + H_{m+1} = \frac{m}{\beta r} (AJ_m(\beta r) + BY_m(\beta r)) \cos \frac{q\pi z}{D}, \quad (24a)$$

$$G_{m-1} - H_{m+1} = (AJ'_m(\beta r) + BY'_m(\beta r)) \cos \frac{q\pi z}{D}, \quad (24b)$$

and substituting these relations into Eqs. (18a) and (18b) we obtain

$$E_\theta = -\frac{q\pi}{D} \frac{m}{\beta r} (AJ_m(\beta r) + BY_m(\beta r)) \left(\sin \frac{q\pi z}{D} \right) e^{-i\omega t + im\theta}, \quad (25a)$$

$$B_\theta = \frac{k^2}{\omega} (AJ'_m(\beta r) + BY'_m(\beta r)) \left(\cos \frac{q\pi z}{D} \right) e^{-i\omega t + im\theta}. \quad (25b)$$

By choosing q to be an integer, i.e., $q = 1, 2, \dots$, the boundary conditions at $z = 0$ and $z = D$ are satisfied. The boundary condition (20a) leads to the relations

$$AJ_m(x_1) + BY_m(x_1) = 0, \quad (26a)$$

$$AJ_m(x_2) + BY_m(x_2) = 0, \quad (26b)$$

where $x_1 = \beta a$ and $x_2 = \beta b$. It is easy to show that the boundary condition (20b) is satisfied when Eqs. (26a) and (26b) are true. The determinant of the algebraic system (26a), (26b) must be zero, and, therefore, the unknown parameter β is determined from the zeroes of the relation

$$J_m(x_1)Y_m(x_2) - J_m(x_2)Y_m(x_1) = 0, \quad (27)$$

for pseudo-TE modes.

Next, let us consider the pseudo-TM modes. A solution of Eq. (17) is

$$G_m(r, z) = \frac{1}{2} (PJ_m(\beta r) + QY_m(\beta r)) \sin \frac{q\pi z}{D}, \quad (28)$$

where β is given by Eq. (23). We choose $H_m(r, z) = G_m(r, z)$, as before, and substituting into Eqs. (19a) and (19b), we obtain

$$B_\theta = \frac{q\pi}{D} \frac{m}{\beta r} (PJ_m(\beta r) + QY_m(\beta r)) \left(\cos \frac{q\pi z}{D} \right) e^{-i\omega t + im\theta}, \quad (29a)$$

$$E_\theta = -\omega \left(PJ'_m(\beta r) + QY'_m(\beta r) \right) \left(\sin \frac{q\pi z}{D} \right) e^{-i\omega t + im\theta}, \quad (29b)$$

for the TM modes. Again, by choosing $q = 1, 2, \dots$, the boundary conditions at $z = 0$, and $z = D$ are satisfied. Either of the boundary conditions (20a), (20b) leads to the algebraic system

$$PJ'_m(x_1) + QY'_m(x_1) = 0, \quad (30a)$$

$$PJ'_m(x_2) + QY'_m(x_2) = 0, \quad (30b)$$

where x_1 and x_2 have been defined. For the pseudo-TM modes, the parameter β is determined from the zeroes of the relation

$$J'_m(x_1)Y'_m(x_2) - J'_m(x_2)Y'_m(x_1) = 0. \quad (31)$$

The final task is the computation of the parameter β from Eq. (27) for the pseudo-TE modes and Eq. (31) for the pseudo-TM modes. This will be done under the assumption that the aspect ratio d/a , where $d = b - a$, is much less than unity. First, let us investigate for zeroes such that the quantity $\delta = x_2 - x_1$ is much less than unity. A Taylor expansion, to third order in δ , of Eq. (27) yields

$$\frac{2d}{\pi a} \left[1 - \frac{1}{2} \frac{d}{a} + \frac{m^2 + 2}{6} \left(\frac{d}{a} \right)^2 - \frac{\delta^2}{6} \right] = 0, \quad (32)$$

and Eq. (31) to second order in δ , yields

$$\frac{2d}{\pi a} \left[1 - \frac{m^2}{x_1^2} - \frac{1}{2} \frac{d}{a} \left(1 - \frac{3m^2}{x_1^2} \right) \right] = 0. \quad (33)$$

These equations are obtained using the identity

$$J_{m+1}(x_1)Y_m(x_1) - J_m(x_1)Y_{m+1}(x_1) = \frac{2}{\pi x_1}, \quad (34)$$

and the recursion formulas for the Bessel functions. Equation (32) does not have a zero for small δ , while Eq. (33) has a zero when $x_1 \approx m$. In this case, we have $\delta \approx md/a$, and for m not very large, the parameter δ is small as originally assumed. More accurately, it follows from Eq. (33) that $x_1 \approx m(1 - d/2a)$. Therefore, when δ is small, the pseudo-TE modes do not have zeroes, while for the pseudo-TM modes $\beta \approx (m/a)(1 - d/2a)$ and from Eq. (23),

$$k^2 = \mu_r \epsilon_r \left(\frac{\omega}{c} \right)^2 \approx \left(\frac{m}{a} \right)^2 \left(1 - \frac{d}{a} \right) + \left(\frac{q\pi}{D} \right)^2. \quad (35)$$

For moderate values of δ and small d/a , the arguments x_1, x_2 of the Bessel functions are large (at this point this is an assumption that will be justified after the zeroes have been computed). Using the asymptotic expressions for the Bessel functions, Eq. (27) gives to lowest order in d/a

$$\delta \tan \delta \approx \frac{4m^2 - 1}{8} \left(\frac{d}{a} \right)^2, \quad (36)$$

while Eq. (31) reduces to

$$\delta \tan \delta \approx \frac{4m^2 + 3}{8} \left(\frac{d}{a} \right)^2. \quad (37)$$

An approximate solution of the relations above can be obtained by setting $\delta = p\pi + \epsilon$, where $p = 1, 2, \dots$, and ϵ is a small parameter. Then Eqs. (36) and (37) have the approximate solutions

$$\delta \approx p\pi + \frac{4m^2 - 1}{8p\pi} \left(\frac{d}{a} \right)^2, \quad (38)$$

and

$$\delta \approx p\pi + \frac{4m^2 + 3}{8p\pi} \left(\frac{d}{a} \right)^2, \quad (39)$$

for values of m that are not very large. From Eqs. (38) and (39) it follows that $x_1 \approx p\pi a/d$ and $x_2 \approx p\pi b/d$, i.e., both x_1 and x_2 are very large and the use of the asymptotic expansions is justified in the derivation of the zeroes. The eigenfrequencies of the psuedo-TE modes can be obtained from Eqs. (23) and (38), and are given by

$$k^2 = \mu_r \epsilon_r \left(\frac{\omega}{c} \right)^2 \approx \left(m^2 - \frac{1}{4} \right) \frac{1}{a^2} + \left(\frac{p\pi}{d} \right)^2 + \left(\frac{q\pi}{D} \right)^2, \quad (40)$$

Similarly, the eigenfrequencies of the pseudo-TM modes can be obtained from Eqs. (23) and (39), and are given by

$$k^2 = \mu_r \epsilon_r \left(\frac{\omega}{c} \right)^2 \approx \left(m^2 + \frac{3}{4} \right) \frac{1}{a^2} + \left(\frac{p\pi}{d} \right)^2 + \left(\frac{q\pi}{D} \right)^2. \quad (41)$$

Eqs. (40) and (41) indicate that the eigenfrequencies for a toroidal rectangular conductor are similar to those of a straight rectangular cavity.

It is apparent from Eqs. (35) and (41) that ω does not vary linearly with m and that the system is dispersive, i.e., the phase velocity is a function of ω . However, when $D \rightarrow \infty$, i.e., for a curved stripline of infinite width satisfying the relation $(b - a)/a \ll 1$, Eq. (35) gives

$$\frac{\omega}{c} \approx \frac{1}{\sqrt{\mu_r \epsilon_r}} \left(\frac{m}{a} \right) \left(1 - \frac{d}{2a} \right),$$

which implies that the phase velocity of the propagating wave is not a function of frequency and thus the various frequency components of the wave propagate with the same speed. Figure 5 shows a sketch of the electric field lines in the stripline. In this geometry, a quasi-TEM mode propagates. The dominant fields are B_z and E_r with a small E_θ component and all other components, namely E_z , B_r and B_θ are zero.

The pulseline described in Section V has a topology different from that of the curved stripline of infinite width and thus it is not clear if the results of the stripline model

are applicable. Obviously, a complete 3-D analysis is required for the actual topology of the toroidal pulseline before a definitive conclusion can be reached about its properties. However, it should be noticed that the wave equation in toroidal geometry is separable in the variables t and θ and thus its solution is a superposition of eigenfunctions of the forms $F(\mu, \xi)e^{i\omega t - im\theta}$, where μ , ξ and θ are the toroidal variables. Unfortunately, the eigenfrequencies of the toroidal pulseline cannot be easily obtained. It is expected that in the general case the pulseline is dispersive. However, for the special case where the separation between the pulseline conductors is much smaller than their minor radii, and the minor radii are also small compared with the major radius of the line, the dispersive effects are likely to be negligible for quasi-TEM modes.

IV. NUMERICAL RESULTS

The beam dynamics in the modified betatron have been studied for the bipolar pulse shown in Fig. 6. The pulse is negative (accelerating) for the first 50 ns, and positive (decelerating) for the subsequent 100 ns. In a Pavlovskii line¹³ only the second pulse is used for acceleration. Here, both the positive and negative polarity components of the pulse are used because more efficient trapping occurs with this choice. The orbit for the beam centroid is obtained by integrating the equations of motion with JAX, a 3-D particle integrator code. The toroidal pulseline electric fields are computed from a cylindrical model with a simple $1/r$ toroidal correction to ensure that $\oint E_{\theta} r d\theta$ is the same for any path. The stellarator fields are calculated from Biot-Savart's law by dividing each period of the winding into twenty segments. The image electric and magnetic fields used in the code have been discussed in previous publications⁷.

Successful trapping in the modified betatron requires that 1) the beam does not hit the injector after the first toroidal revolution around the major axis and 2) the beam does not return to the injector after a poloidal (bounce) period. Numerical results for various amplitude pulses are shown in Figs. 7, 8 and 9. The parameters for the three runs are listed in Table I. The figures show the projection of the beam centroid on the $\theta = 0$ plane. The small circular motion in these figures is associated with the stellarator field (intermediate frequency mode). Since there are six stellarator field periods between $0 \leq \theta \leq 2\pi$, the beam centroid performs six oscillations during a revolution around the major axis. The beam moves approximately 1 m in the toroidal direction for each small orbit.

Results with the 80 kV bipolar pulse are shown in Fig. 7. At the end of the first revolution around the major axis ($t \approx 25$ ns), the beam has moved almost 5 cm which is more than enough to miss the injector and its shroud. At the end of the first bounce period, the beam is on an orbit with a radius of just over 3 cm centered at 100.6 cm. Thus both trapping criteria have been met.

As the beam passes through the gap, its energy changes. This change in γ will cause the center of the bounce (slow) motion to move according to

$$\frac{\Delta r}{r} = \frac{\Delta \gamma / \gamma}{n - n_s(r_b/a)^2 + n_{sf}},$$

where $\Delta \gamma$ is the energy mismatch, n is the external field index, n_s is the self field index, n_{sf} is the strong focusing index¹⁰, r_b is the beam radius, and a is the minor radius of the vacuum chamber.

For the parameters of Fig. 7, Δr is ± 0.9 cm. Its sign depends on the polarity of the pulse. At $t = 0$ the center of the bounce motion is at $r = 102.4$ cm. After $t = 50$ ns, the electron beam has been accelerated twice by the negative voltage and the equilibrium position is at 104.2 cm. This change in the center of the motion results in a smaller radius of curvature than it would have otherwise. During the second (positive) phase of the bipolar pulse, the beam is decelerated 4 times with a net change in equilibrium position of 3.6 cm and the center of the orbit is at 100.6 cm. The bipolar pulse, properly timed, has the effect of chasing the particle and continuously decreasing the size of the orbit.

An even better final orbit is obtained by increasing the pulseline voltage to 100 kV as shown in Fig. 8. Because of the larger $\Delta\gamma$ the final equilibrium position is at 100.2 cm and is closer to the beam. The final radius of the poloidal orbit is considerably larger when the amplitude of the bipolar pulse is reduced to 60 kV, as shown in Fig. 9. If the toroidal field and the strong focusing current are halved, the required bipolar pulse amplitudes are also roughly halved for similar trapping characteristics. However, the beam radius r_b is larger at the lower toroidal field.

V. PULSELINE CONSTRUCTION

The modified betatron vacuum chamber consists of twelve flange coupled 30° sectors with a major radius of 100 cm, and a minor radius of 15 cm. The pulseline was designed as an integral part of a 60° sector, and it is intended to replace two 30° vacuum chamber sectors. Fig. 10 shows a simplified drawing of the pulseline. The insulating spacer across which the gap voltage is developed is shown at the leftmost end. The pulseline looks like a toroidal coaxial equivalent of a folded stripline. The radii of the inner and outer conductors

are $R_1 = 16.8$ cm and $R_3 = 21.6$ cm. The radius R_2 of the middle conductor is chosen to make the characteristic impedance between the inner and middle conductors equal to that between the outer and middle conductors. Thus $R_2 = \sqrt{R_1 R_3} = 19.0$ cm. The choice of values for R_1 and R_3 is severely limited by the available space between the vacuum chamber and the coils of the modified betatron.

Deionized water is used as the dielectric medium between the pulseline conductors. This choice yields the maximum practical pulselength for given geometric dimensions. Since the dielectric constant of water is ~ 80 , the mean one-way transit time τ is 45 ns. To avoid field errors, the magnetic field penetration time of the pulseline needs to be the same as for the rest of the vacuum chamber. The pulseline is constructed from fiberglass and epoxy-reinforced carbon fibers. The modified betatron vacuum chamber is constructed similarly. The inner pulseline conductor is made of seven layers of carbon fiber cloth with a total thickness of 1.5 mm. However, a major portion of the line current is carried by a sheet of phosphor-bronze wire cloth embedded between the outer two carbon layers. The surface resistivity of the wire cloth is $32 \text{ m}\Omega$ on a square. The measured resistivity of the carbon fiber matrix is $\sim 8 \text{ m}\Omega\text{-cm}$. The middle conductor is also made of carbon fiber with an overall thickness of 1.5 mm, but it has two sheets of phosphor-bronze wire cloth to simulate the folded nature of the pulseline. Finally, the outer conductor is similar in construction to the inner conductor.

The middle conductor is perforated with a large number of 3-mm-diam. holes to facilitate free circulation of water within the pulseline. The hole spacing is ~ 2.5 cm. Water is admitted through five holes at the bottom. After circulating through the pulseline, the

water exits through five holes at the top, and then passes through a deionizer before returning to the inlet holes. The water resistivity is maintained above $8 \text{ M}\Omega\text{-cm}$. Also, the initial filling is done gradually, typically taking 20-30 minutes. This minimizes bubbles in the pulseline and in the circulating water.

Switching is done by a set of triggered vacuum surface flashover switches. Cast polyurethane annular disks separate the vacuum flashover region from the outside, and from the water dielectric medium. Spark gap switches cannot be used here for several reasons. The capacitance of the middle conductor with respect to the inner and outer conductors is 50 nF . For a typical charge voltage of 20 kV , the stored energy in the pulseline is only 10 J . It is doubtful if spark gaps can switch the pulseline with a total switch resistance loss less than 0.5 J . Another disadvantage of spark gaps is their inability to perform at low voltages as crowbar switches. Ideally, during the crowbar phase, the switch needs to close when there is no voltage between its electrodes. The vacuum surface flashover switches used here perform admirably well under these conditions as will be shown in the next section. Because of the tight space restrictions, a spark gap switch might take the form of an annular rail-gap switch. But the machining tolerances that would be necessary to ensure multichannel operation at these low voltages, would be quite impractical for a rail-gap switch. The surface flashover switches also offer the added convenience of almost complete isolation between the trigger and pulseline charge circuits.

Eight surface flashover sites on the vacuum side of the outer polyurethane disk initiate pulse propagation in the water lines. Each site is triggered by plasma emanating from the end of an overvolted 0.64-cm-diam. semi-rigid coaxial cable. A simplified circuit diagram of

the initiation driver circuit is shown in Fig. 11. The spacing between the end of the trigger coax and the polyurethane surface is typically 8 mm. The inductance of each flashover switch is roughly 50 nH. If all eight switches fire synchronously, the net inductance is $50/8 = 6.3$ nH. Using Eq. (5) the pulseline characteristic impedance is 0.84Ω . So the risetime due to inductance alone is $2.2 \times 6.3/0.84 = 16.5$ ns. The crowbar switches are a similar set of eight triggered flashover sites on the inner polyurethane disk. The crowbar driver circuit is also similar to the initiation circuit shown in Fig. 11. All electrical connections between pulseline conductors are made via spiral wound RF gaskets. Gold plated, 1.3-cm-wide stainless steel strips on the conductor walls provide the mating surfaces for the RF gaskets.

Four capacitive probes in the outer conductor wall monitor the electric field between the middle and outer conductors. Each probe is a gold plated stainless steel disk with a diameter of 1.25 cm. The probe surface is in intimate contact with the water and is flush with the inside surface of the outer conductor. Thus field perturbations due to these probes are kept to a minimum. Of the four probes, two namely CAP1 and CAP4 are on the horizontal midplane. CAP1 is the capacitive probe closest to the initiation switches. Its distance from the switching plane, measured along the inside surface of the outer conductor, is ~ 27 cm, and the distance of CAP4 from the switching plane is ~ 80 cm. The probes CAP2 and CAP3 are located midway between the other two probes, but CAP2 is displaced 60° in poloidal angle above the horizontal midplane, and CAP3 is 60° below the midplane. Their distance from the switching plane is ~ 53 cm.

VI. EXPERIMENTAL RESULTS

Before discussing the pulseline results, it is instructive to review some of the results obtained from an earlier experiment set up to study the characteristics of the vacuum surface flashover switch. A 2.5-cm-high block of polyurethane supported between brass plates, formed the flashover switch for this experiment. The plates were connected to a 3-m-long semi-rigid coaxial cable charged to 30 kV. Plasma from another overvolted semi-rigid coaxial cable triggered the main switch. The driver circuit for the trigger coax is similar to that shown in Fig. 11, and typical charging voltages ranged from 15 kV to 30 kV. The flashover switch current was measured with a shielded Rogowski coil. The risetime appeared to be ~ 10 ns. The calculated rise time due to switch and lead inductances is only 5 ns. Thus a substantial part of the rise time needs to be attributed to the resistive phase of the switch. Resistive rise times usually depend on the magnitude of the voltage across a switch, while inductive rise times show no such dependence. The presence of the resistive phase was confirmed when the rise time increased to 20 ns for charge voltages below 15 kV. For a 10 mm spacing between the trigger coax end and the flashover surface, switch current was observed roughly 50 ns after the trigger coax end overvolted. This delay may be attributed to the finite plasma propagation velocity, which appears to be on the order of 10^7 cm/s. When the spacing was increased to 13 mm the delay increased to ~ 65 ns, and for a spacing of 6 mm the delay appeared to be ~ 35 ns. The switch voltage was 30 kV and the driver charge voltage was -25 kV. The switch performance showed a weak dependence on the polarities of these voltages. The sixteen initiation and crowbar switches used on the pulseline are roughly similar in dimensions to the switch described above. Thus comparable performance can be expected.

The pulseline cannot be dc charged because of resistive losses due to the relatively high water conductivity. For a 20-kV charge voltage, the resistive loss in the pulseline is 1.3 J if the voltage is applied for 4 μ s and the water resistivity is 8 M Ω -cm. This needs to be compared with the 10 J stored energy in the electric fields. The pulse charge time is therefore chosen to be less than 2 μ s, and the charge voltage is near its maximum only for about 1 μ s. Figure 12(a) shows the charging voltage on the middle conductors as measured by capacitive probe CAP1. The pulse charge circuit consists of an 80-nF capacitor dc charged to 18 kV and discharged by a spark gap into a short length of coaxial cable the other end of which connects to the middle and outer pulseline conductors. Since the pulseline capacitance is 50 nF, the charging waveform is expected to have a $[1 - \cos(\omega t)]$ dependence, which appears to be the case in Fig. 12(a), and the peak voltage is $18 \times 2 \times 30.8/50 = 22$ kV. The equivalent series inductance is ~ 8.7 μ H.

The initiation switches fire at ~ 2 μ s when the charge voltage reaches its peak. A gap voltage appears immediately after initiation as shown in Fig. 12(b). The gap voltage is shown on an expanded time scale in Fig. 13(b). It is measured using a capacitive probe located close to the insulating gap spacer. The signals in Fig. 12 are integrated with a 10- μ s passive integrator. For the waveforms in Figs. 12 and 13, the pulseline is not crowbarred and there is no load (beam current). When the initiation switches fire, a quasi-TEM wave is excited in the outer water line. The wavefront propagates away from the switches until it reaches the end of the middle conductor. Here the wave makes a 180° turn and most of the wave energy propagates in the inner water line toward the crowbar switches. Because of the open-circuit condition at the gap, the wave reflects and proceeds towards the initiation switches where it reflects again because of the short-circuit, and the

cycle repeats. The period of the cycle is the two-way transit time in the pulseline, i.e., 90 ns.

The gap voltage in Fig. 12(b) appears to decay with an e-folding time of 0.7 μ s. The decay rate can be calculated from the known resistivities of the conductors used. The gap voltage is obtained by integrating the rate of change of the magnetic flux enclosed by the dashed line in Fig 1. This voltage is also equal to the magnitude of the propagating voltage wavefront, if a one-dimensional approximation is employed for the pulseline. A propagating wavefront in an infinitely long line is described by $V \exp(-\gamma z)$, where $\gamma^2 = (R + Ls)(G + Cs)$. R , L , G and C are the line resistance, inductance, conductance and capacitance per meter and s is the Laplace transform time variable. Since the gap voltage is roughly sinusoidal after the first oscillation, one can substitute $j\omega$ for s and write $\gamma = \alpha + j\beta$, where $\omega/2\pi$ is the frequency of the oscillation. If $R \ll \omega L$ and $G \ll \omega C$, $\alpha \cong R/(2Z_o) + GZ_o/2$, where $Z_o = \sqrt{L/C}$. Using the known resistivities for the carbon-fiber matrix and the phosphor-bronze screen, $R = 33.5 \text{ m}\Omega/\text{m}$. G can be used to account for losses in the water. For a resistivity of 8 $\text{M}\Omega\text{-cm}$, the conductance G is $6 \times 10^{-4} \text{ mho/m}$, and since $Z_o = 0.84 \Omega$, the attenuation constant α is 0.02 Neper/m. Losses in water account for only 1.3% of the total losses. The calculated value of α predicts an e-folding time of 1.5 μ s for the decay rate of the gap voltage. This is roughly twice the observed time in Fig. 12(b).

The higher resistive losses in the experiment may be due to several factors. Potential sources for this discrepancy include joint resistances, perforations in the middle conductor, additional losses when the wave makes the 180° turn around the edge of the middle con-

ductor, losses in the switches, and losses due to skin effect. The correction for skin effect is likely to be small because the diameter of the individual wires forming the phosphor-bronze screen, is $38\text{ }\mu\text{m}$, while the skin depth for the dominant frequency is $\sim 50\text{ }\mu\text{m}$.

Figure 13 shows the pulseline waveforms on an expanded timescale. Only the initiation switches fire for this sequence of shots. Figure 13(a) shows the current in one of the trigger coaxes at the driver end of the line (see Fig. 11). The current is measured using a shielded Rogowski coil and integrated with a passive $2\text{-}\mu\text{s}$ integrator. This waveform triggers the oscilloscope and serves as the time reference for all other waveforms in Fig. 13. The dc charge voltage on the 80-nF driver capacitor is -24 kV . Waveforms (b) thru (e) are integrated with a $10\text{-}\mu\text{s}$ passive integrator. Figure 13(b) shows a two-shot overlay of the gap voltage. The dip at 330 ns does not appear to be quite reproducible, probably because of variations or lack of synchronism in the initiation switch firings. Waveforms (c), (d) and (e) show the voltages measured by capacitive probes CAP1, CAP3 and CAP4. There is a certain amount of shifting of the zero-level baseline in these signals. This is readily apparent in Fig. 12(a), and it is due to the inadequate RC time of the $10\text{-}\mu\text{s}$ integrator. This effect is absent in the gap voltage waveforms because they are approximately symmetrical voltages. Signals (b) thru (e) use a common-mode rejector¹⁵ while (a) does not. The common-mode rejector was made by winding 97 turns of RG-174 cable on a ferrite core, and it adds a delay of 90 ns . Additionally, since the Rogowski coil measures the current at the driver end, it can "sense" the trigger coax flashover event only after 45 ns , which is the one-way transit time of the trigger cables. The flashover event occurs at $t = 120\text{ ns}$ in Fig. 13(a), and the gap voltage appears at $t = 230\text{ ns}$ in Fig. 13 (b). The delay in the firing of the initiation switches is therefore $(230 - 120) - (90 - 45) = 65\text{ ns}$. This is consistent with

the finite plasma propagation velocities and delays measured for the prototype flashover switch described at the beginning of this section.

The rise time of the gap voltage waveform in Fig. 13(b) appears to be ~ 22 ns as indicated by the first negative going pulse. This could be the result of only six out of eight switches firing simultaneously, in which case the predicted risetime is $2.2 \times 8.3 / 0.84 = 22$ ns. Because of the transit time isolation between switches, there is a high probability that all eight switches fire on every shot, but two switches may fire, say 5 ns later. This is a likely event, in view of the fact that the delay due to trigger plasma propagation time, is roughly 65 ns. A more detailed comparison of the waveforms in Fig. 13 with simulated waveforms, is carried out in the next section.

Figure 14 shows the effect of crowbarring. The delay between the initiation and crowbar switch firings can be continuously varied. Figure 14(a) shows the gap voltage when the crowbar switches fire at the right time. The waveform is close to the desired waveform (see Fig. 6). In Fig. 14(b) the pulseline was crowbarred ~ 20 ns later. The delay can be arbitrarily varied to essentially short-circuit the gap voltage at any point in time. Even though there is energy stored in the pulseline during the post-crowbar phase, no gap voltage appears because both ends of the line have been short-circuited. Figure 14(a) appears to indicate that the flashover switches perform satisfactorily even when there is very little voltage across them. It is extremely difficult to achieve similar performance with spark gaps.

Following the installation of the strong focusing windings in the NRL device it has been routinely observed that for several combinations of injection parameters, the beam consis-

tently spirals from the injection position to the magnetic minor axis and is trapped.^{1, 12} Thus, trapping experiments using the pulseline have not yet been performed. If successful, the trapping of the beam with the pulseline is expected to make the modified betatron more versatile because it will allow a wider choice of the values of the toroidal and strong focusing fields during injection.

VII. DISCUSSION

In this section, the experimental data are compared with results from a computer simulation for a straight coaxial transmission line, which is known to obey the one dimensional wave equation. An interesting outcome of this comparison is the possibility that three dimensional effects in the toroidal pulseline counteract some of the distortions in pulse shape due to switch inductance. The net result is a superior pulse shape in comparison with the pulse that would have been obtained with a straight coaxial pulseline.

There are several features in the experimental data that do not agree with the computer simulations. These differences are described in more detail later in this section. The gap voltage waveform (Fig. 13 (b)) is of special interest. Although, the initial falling edge of the bipolar gap voltage waveform indicates a rise time of ~ 22 ns, which is close to the predicted value, the subsequent rising edge at ~ 300 ns lacks a "shoulder" and has a rise time of ~ 32 ns which is much larger than expected. Also, the dip at ~ 350 ns is considerably smoothed out. These, and other smoothing effects become apparent when waveforms (b) thru (e) in Fig. 13 are compared with the simulated waveforms appearing in Fig. 16.

The 1-D simulations are performed using a transmission line code that is routinely

used for the analysis of transient in electrical circuits. The code successfully reproduces the current waveform in Fig. 13(a), where wave propagation takes place in a 9-m long, RG-214 coaxial cable, and three dimensional effects are absent. Figure 15 shows the transmission line representation of the toroidal pulseline, as used in the 1-D code. The voltages V_1 , V_3 and V_4 at the junction nodes correspond to the voltages measured by the capacitive probes CAP1, CAP3 and CAP4, and the electrical lengths of the four transmission lines are appropriately chosen. Also, $\sum_{i=1}^4 \tau_i = 45$ ns, which is the one-way transit time of the pulseline. All lines are assumed to be lossless. The switch inductance L_s is assumed to be 8 nH, corresponding to the case where six out of eight switches fire simultaneously.

The topology of the pulseline is interesting in the sense that the gap voltage responds immediately to the closure of the initiation switches. Therefore, the rise time of the gap voltage is directly related to the switch closure time. Figure 16(a) shows that the rise time of the first negative going pulse is ~ 25 ns, which agrees with the experimental value. However, the fall time of the negative pulse shows a well defined shoulder at ~ 45 ns. This shoulder is absent, or is considerably smoothed out in the experiment (see Fig. 13(b)). The shoulder occurs when the propagating wavefront reaches the crowbar switches, and reflects due to the open circuit condition at the gap. The dispersive resistive losses in the pulseline can also cause smoothing, but this is not applicable here because resistive losses modify the pulse shape only over long periods of time, while the smoothing described above occurs almost instantaneously. Traces (b), (c) and (d) in Fig. 16 show the calculated voltages corresponding to those measured by capacitive probes CAP1, CAP3 and CAP4. These waveforms show well defined shoulders (for example, the shoulder in (b) is at ~ 85 ns),

which are delayed signatures of the reflection event at the gap. Again, all these shoulders are smoothed out in the experimental data.

Another distinguishing feature is the large dip in the calculated gap voltage waveform in Fig. 16(a) at ~ 100 ns. This occurs when the wavefront returns to the initiation switches and reflects. The dip would be absent if an ideal, distributed, radial switch with zero inductance is employed in place of the eight surface flashover switches used in the experiment. If the switch inductance L_s is reduced, the depth of the dip is unaffected, but its width is reduced. This can also be shown analytically. The gap voltage dip is considerably smoothed out in the observed waveform.

An explanation of the observed smoothing is the possibility that the three dimensional geometry of the pulseline causes substantial wavefront distortions, and the toroidal pulseline may indeed be dispersive. There may also be other mechanisms that distort the waveforms in the experiment. However, the distortions cannot be attributed to the capacitive probes used for the measurements, because these probes are known to have adequate frequency response. In an earlier analysis of curved transmission lines,¹⁶ expressions for the characteristic impedance of a deformed line have been derived, but the analysis does not treat the details of wave propagation inside the line. It is well known that a sharp bend in a coaxial cable distorts the shape of a pulse sent through it. The distortion is usually analyzed in terms of the impedance mismatch introduced by the bend. In practice, mechanical considerations limit the bend radius of cables. As a result, the observed distortions in cables are usually negligibly small.

The gap voltage waveform of a straight coaxial pulseline is expected to have a pro-

nounced dip as shown in Fig. 16(a). This dip is considerably smoothed out in the toroidal pulseline and the gap voltage waveform bears closer resemblance to the ideal waveform. The accelerated electron beam interacts with the pulseline only via the gap voltage and the beam cannot "sense" the higher order modes or other nonideal conditions existing inside the pulseline. So, in a restricted sense, the toroidal pulseline might be superior to a straight coaxial pulseline.

VIII. SUMMARY AND CONCLUSIONS

Numerical results from the integration of orbit equations indicate that the injected electron beam in a modified betatron accelerator can be trapped using a charged pulseline over a wide range of operating parameters. Trapping is accomplished by modifying the poloidal orbit within a bounce period. This orbit modification is due to the change of beam energy. A distinctive feature of this trapping scheme is that the average canonical angular momentum $\langle P_\theta \rangle$ is not conserved. Trapping is achieved over a wide range of pulseline voltages from 30 kV to 100 kV.

A toroidal coaxial version of the Pavlovskii line is used to change the energy of the beam. A $0.84\text{-}\Omega$ water dielectric line has been built and tested. The toroidal pulseline is successfully switched using triggered vacuum surface flashover switches. The rise time of the crowbarred, bipolar pulse is typically 22 ns. The gap voltage waveform of a straight coaxial pulseline is expected to have a pronounced dip due to switch inductance. Experimental data show that this dip is considerably smoothed out in the toroidal pulseline.

REFERENCES

1. C. A. Kapetanakis *et al.*, Phys. Rev. Lett. **64**, 2374 (1990).
2. H. Ishizuka *et al.*, in *Proceedings of the Seventh International Conference on High-Power Particle Beams, Karlsruhe, Germany, 1988*, edited by W. Bauer and W. Schmidt (Kernforschungszentrum Karlsruhe GmbH, Karlsruhe, 1988), Vol. II, p. 857.
3. S. Humphries, Jr., and L. K. Len, in *Proceedings of the 1987 Particle Accelerator Conference, Washington, D.C., 1987*, edited by E. R. Lindstron and L. S. Taylor (IEEE, New York, 1987), p. 914.
4. V. Bailey *et al.*, in *Proceedings of the 1987 Particle Accelerator Conference* (Ref. 3), p. 920.
5. W. K. Tucker *et al.*, in *Proceedings of the 1987 Particle Accelerator Conference* (Ref. 3), p. 957.
6. P. Sprangle and C. A. Kapetanakis, J. Appl. Phys. **49**, 1 (1978).
7. C. A. Kapetanakis *et al.*, Phys. Fluids **26**, 1634 (1983).
8. N. Rostoker, Comments Plasma Phys. **6**, 91 (1980).
9. C. Roberson *et al.*, Phys. Rev. Lett. **50**, 507 (1983).
10. C. A. Kapetanakis *et al.*, Part. Accel. **21**, 1 (1987).
11. P. Sprangle and C. A. Kapetanakis, Part. Accel. **18**, 203 (1986); Y. Seo and P. Sprangle, *ibid.* (to be published).
12. C. A. Kapetanakis *et al.*, Phys. Rev. A. **44**, 3900 (1991).

13. A. I. Pavlovskii *et al.*, Sov. Phys. Dokl. **20**, 441 (1975).
14. D. Eccleshall and J. K. Temperley, J. Appl. Phys. **49**, 3649 (1978).
15. J. Mathew, Rev. Sci. Instrum. **61**, 1926 (1990).
16. H. H. Meinke, Arch. Elekt. Über. **5**, 106 (1951).

Table I. Parameters used for the beam trapping simulations.

	Fig. 7	Fig. 8	Fig. 9
Relativistic factor γ	2.36	2.36	2.36
Bipolar pulse amplitude (kV)	∓ 80	∓ 100	∓ 60
$\Delta\gamma/\text{pass}$	± 0.157	± 0.196	± 0.117
Beam current I_b (kA)	1.36	1.36	1.36
Injection radius r_i (cm)	108	108	108
Beam radius r_b (cm)	1	1	1
Self field index $n_s(r_b/a)^2$	0.6	0.6	0.6
Torus major radius r_o (cm)	100	100	100
Torus minor radius a (cm)	15.2	15.2	15.2
SF radius ρ_o (cm)	23.4	23.4	23.4
SF current I_{sf} (kA)	20	20	20
SF index n_{sf}	8	8	8
Vertical field at injection B_z (G)	34	34	34
Vertical field index n	0.5	0.5	0.5
Toroidal Field B_θ (G)	4000	4000	4000

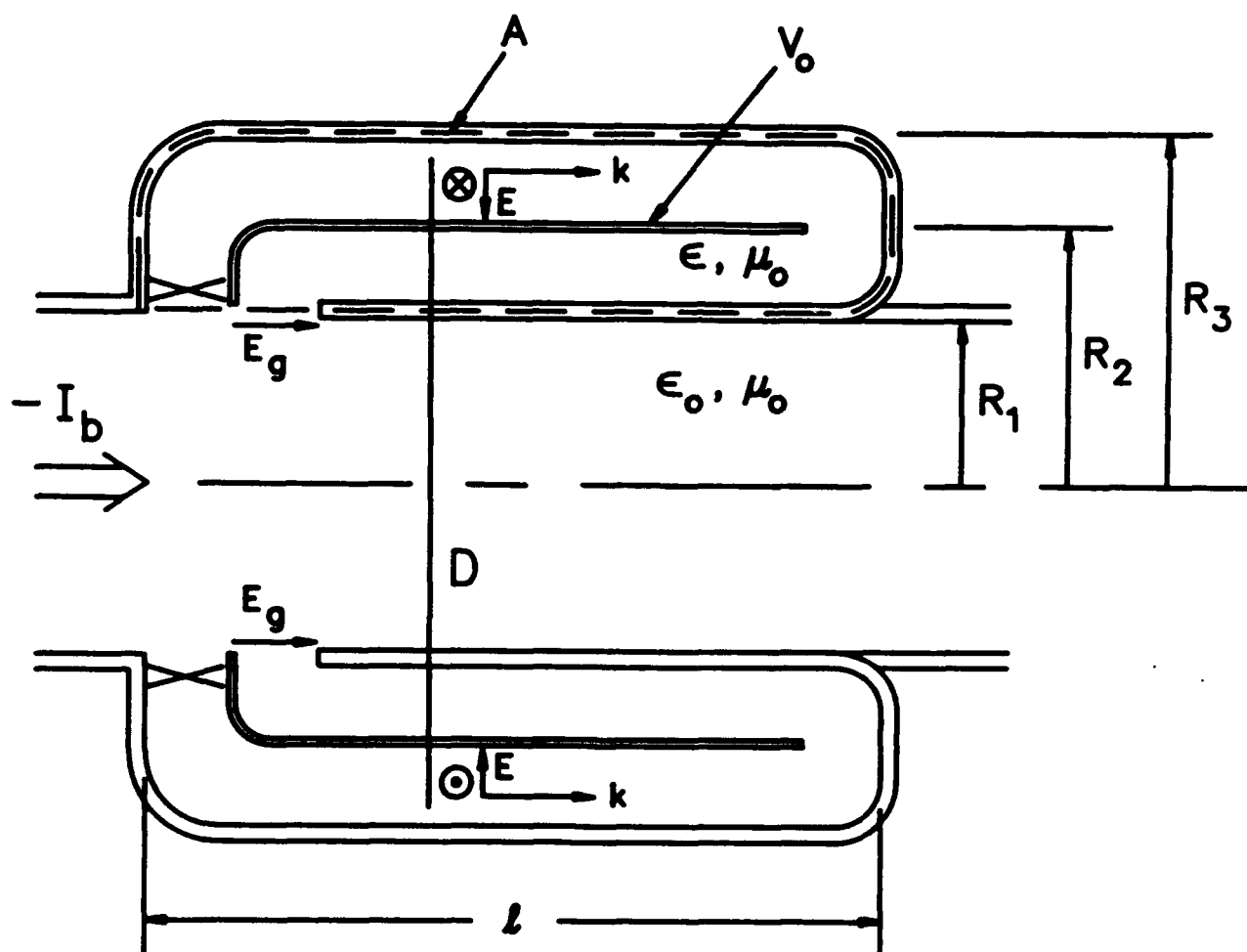


FIG. 1. Simplified cross sectional view of the coaxial pulseline.

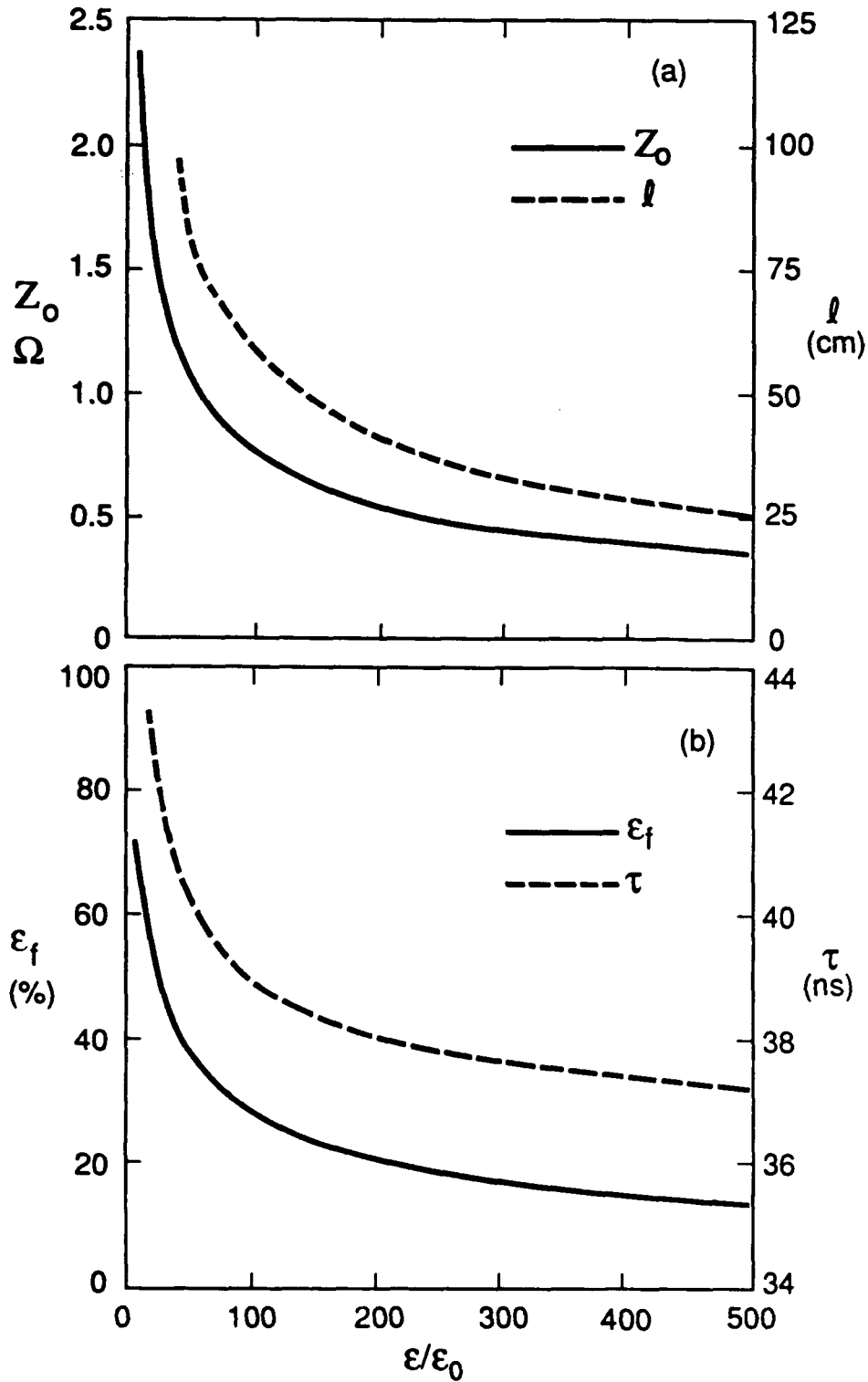


FIG. 2. Pulseline characteristics for $\Delta E = 60$ keV, $\tau_o = 24$ ns, $V_o = 20$ kV, $I_b = 2$ kA, $R_1 = 16.8$ cm, $R_2 = 19.0$ cm and $R_3 = 21.6$ cm. (a) Plots of Z_o and ℓ versus ϵ/ϵ_o . (b) Plots of ϵ_f and τ versus ϵ/ϵ_o .

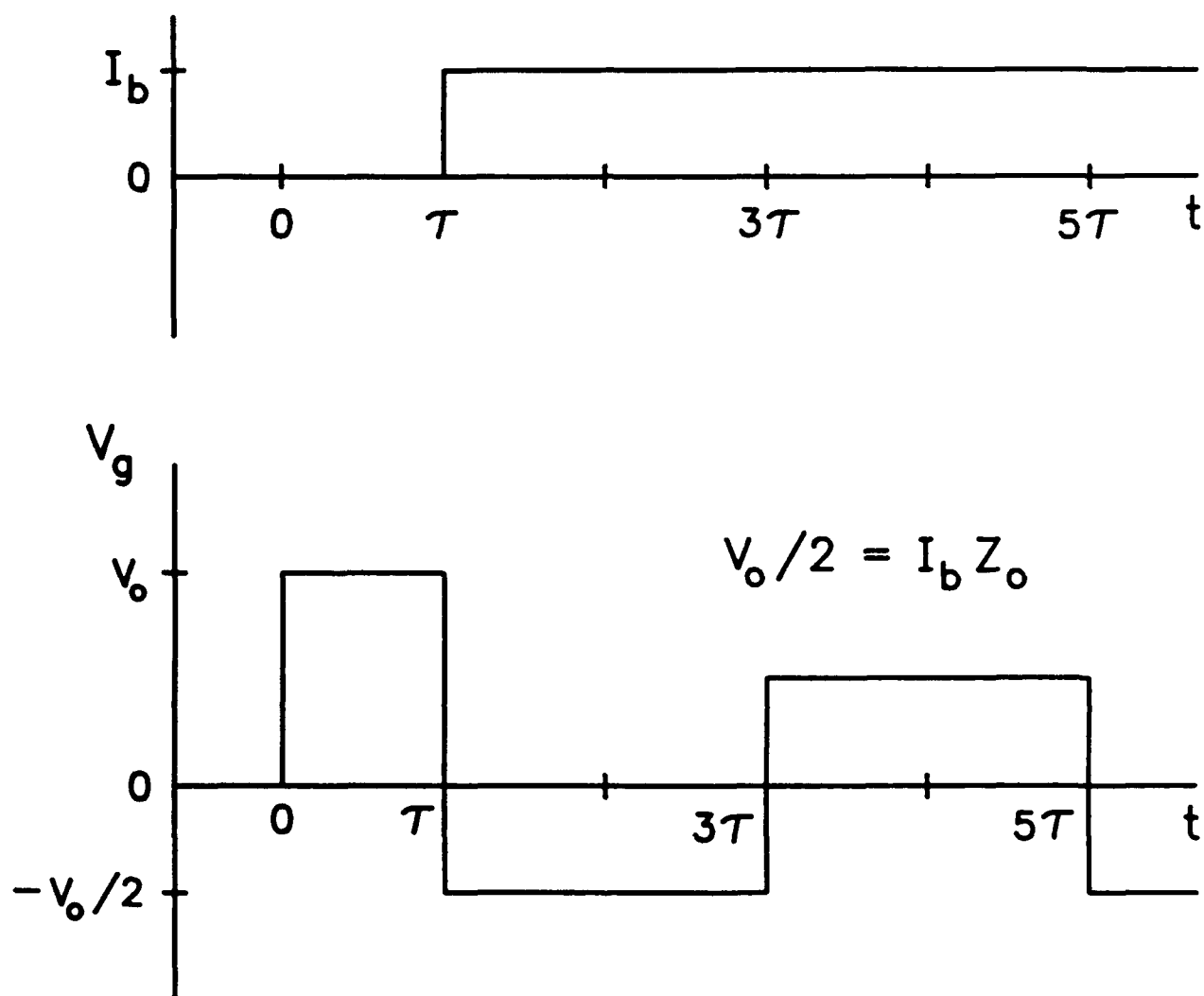


FIG. 3. Injected beam current and gap voltage waveforms for the matched condition.

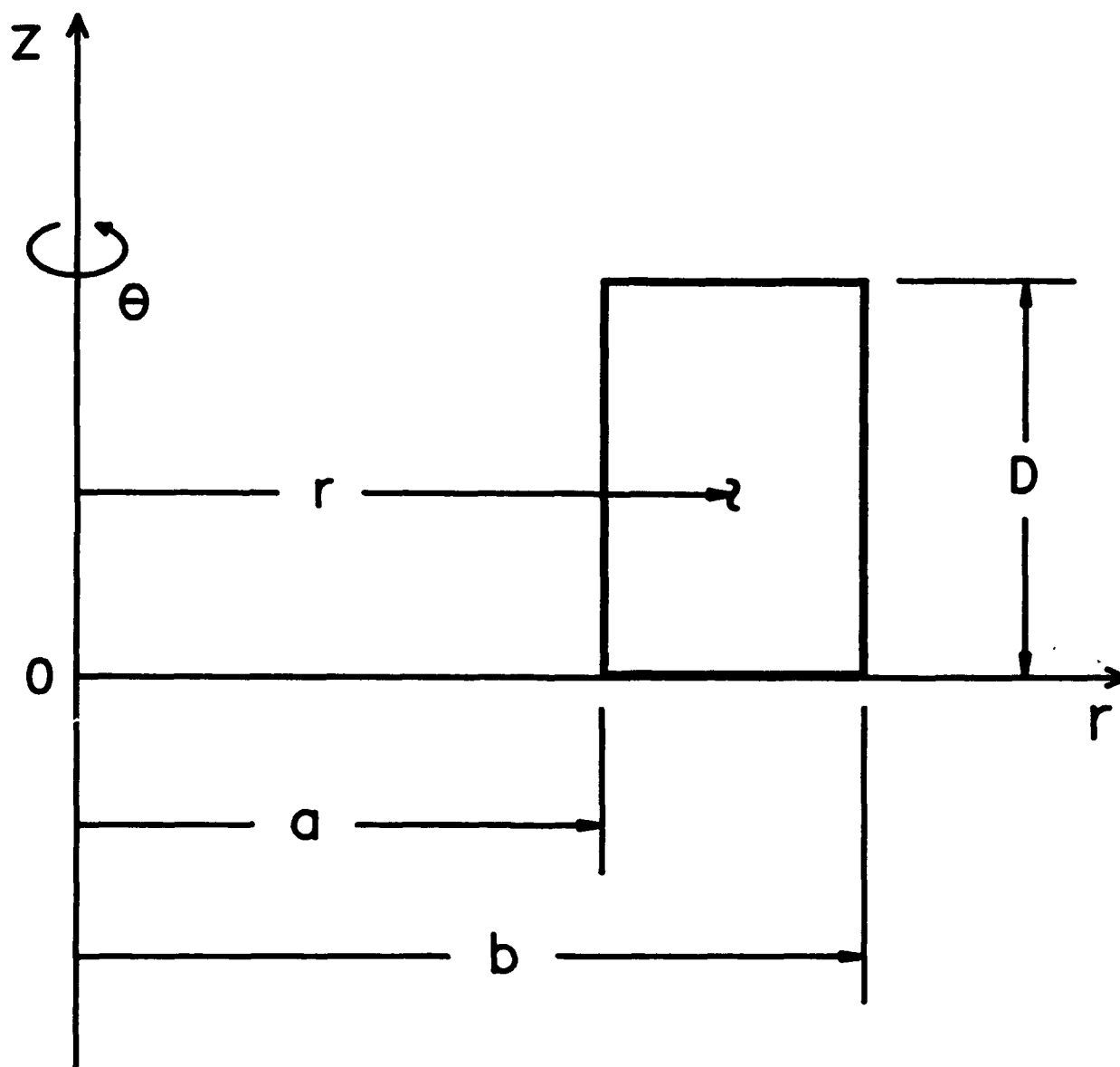


FIG. 4. Coordinate system for a toroidal waveguide with rectangular cross section.

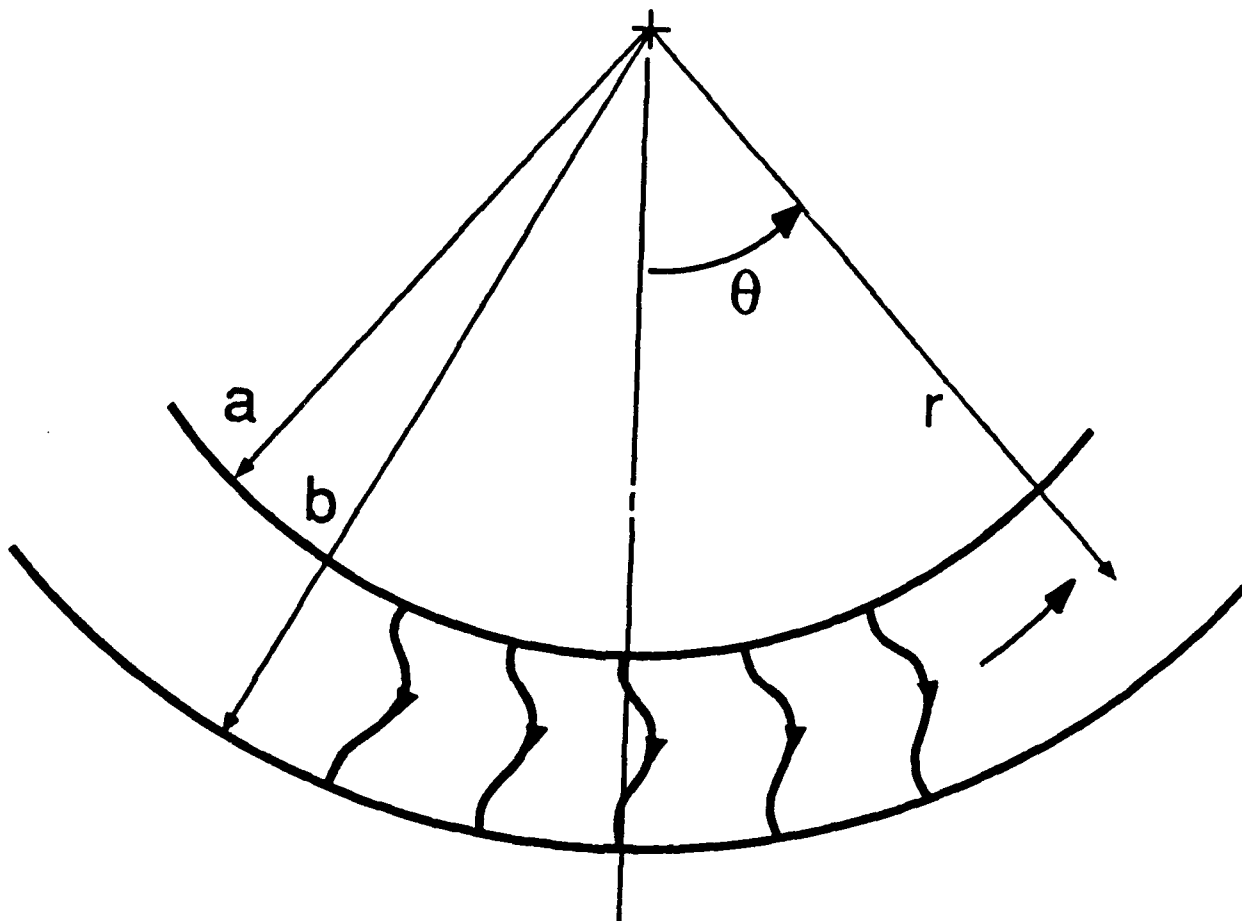


FIG. 5. Sketch of quasi-TEM wave propagation in a curved stripline of infinite width.

Only electric field lines are shown, and E_θ is shown exaggerated for clarity.

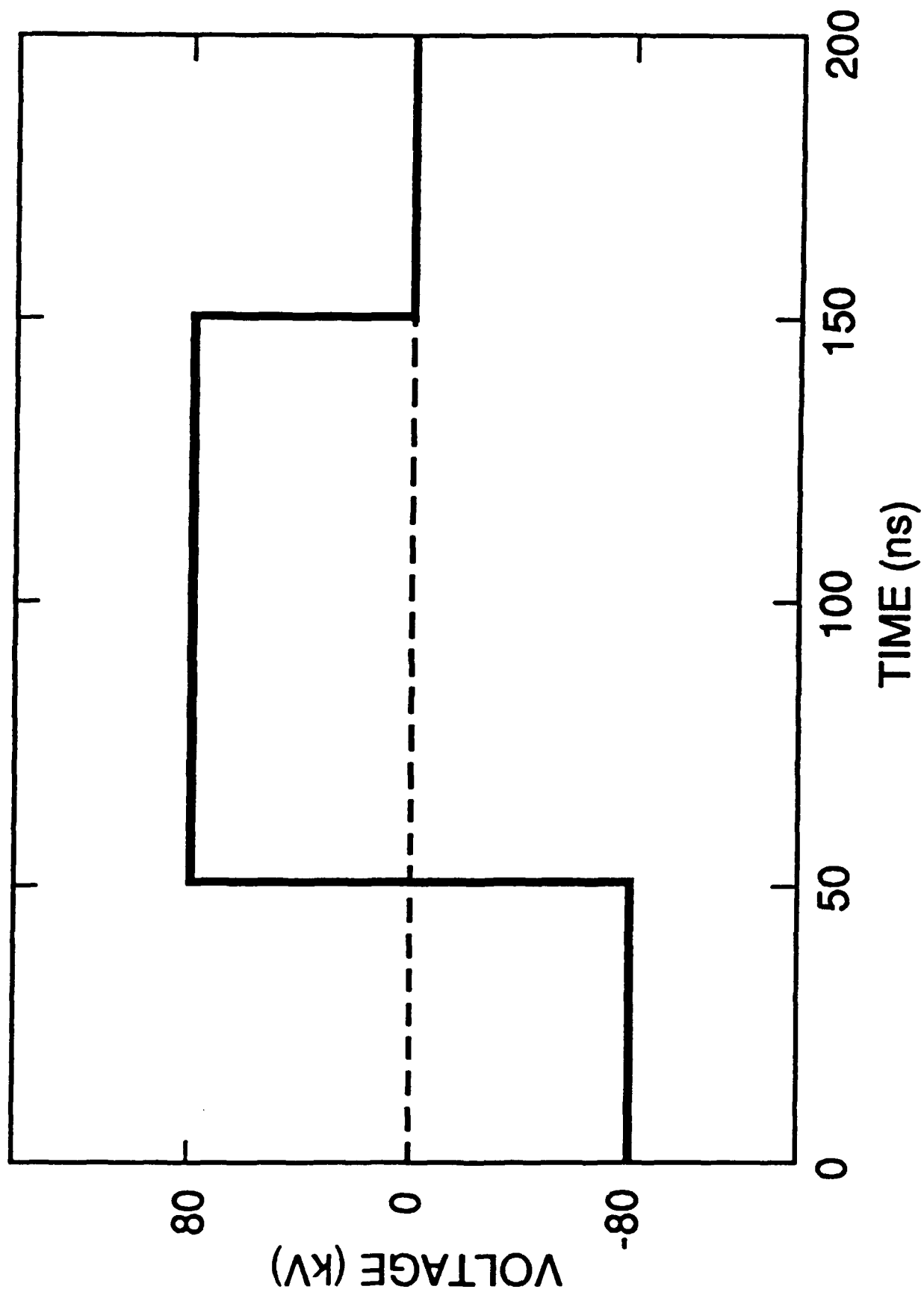


FIG. 6. Bipolar gap voltage pulse used for numerical simulations.

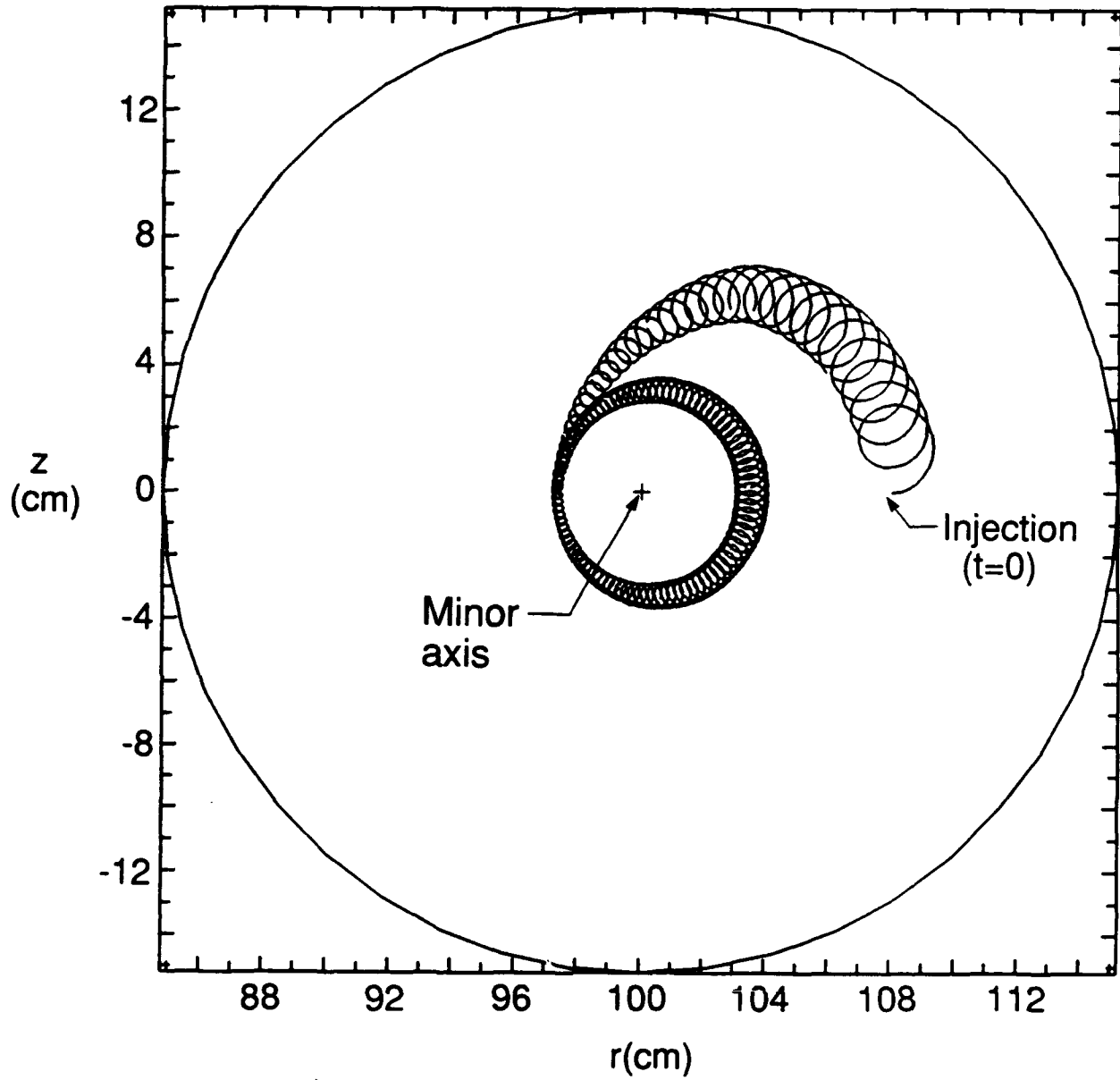


FIG. 7. Beam trapping simulation for an 80-kV bipolar pulse. The minor axis is at $r = 100$ cm. Other parameters are listed in Table I.

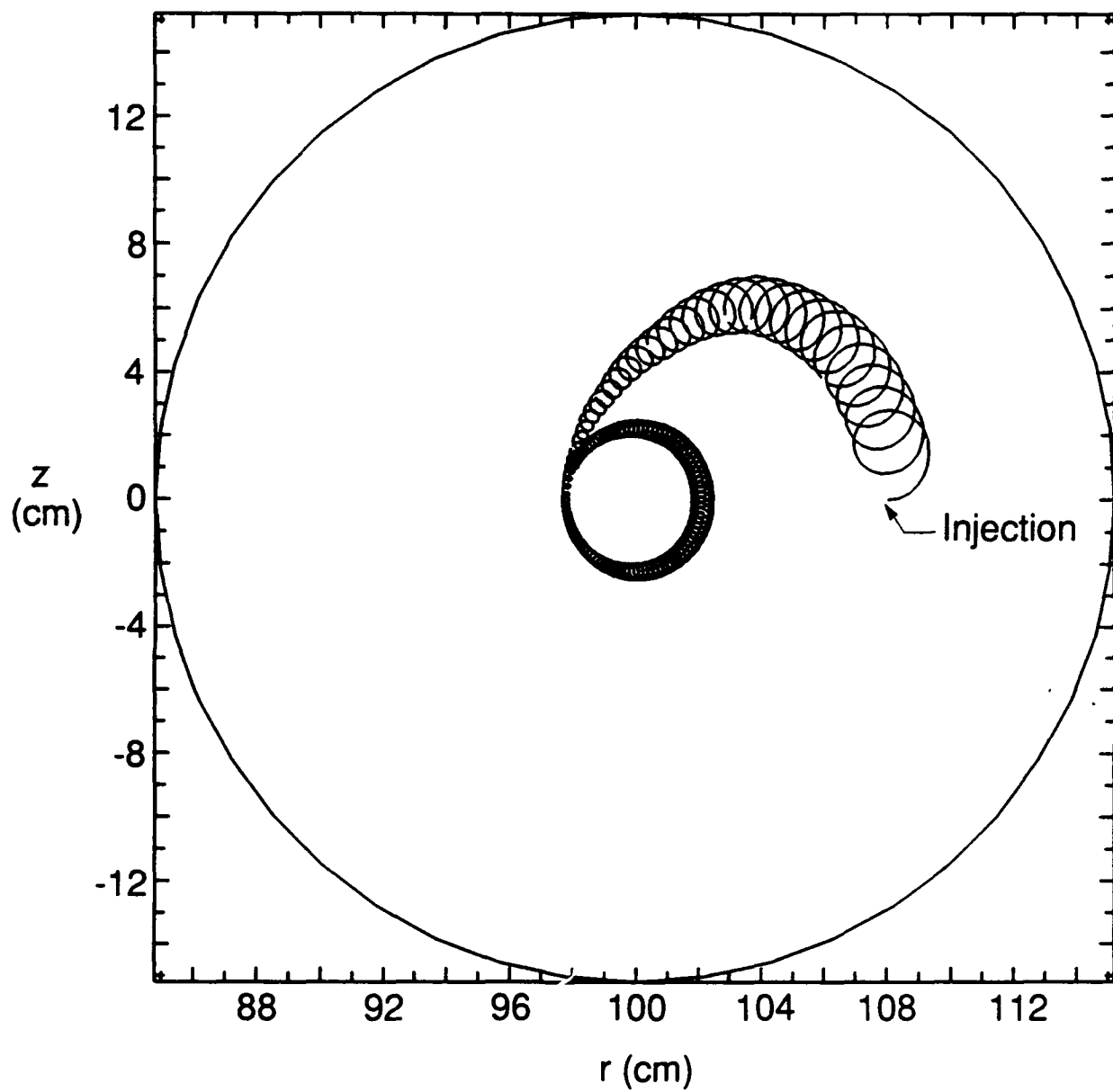


FIG. 8. Beam trapping for a 100-kV pulse.

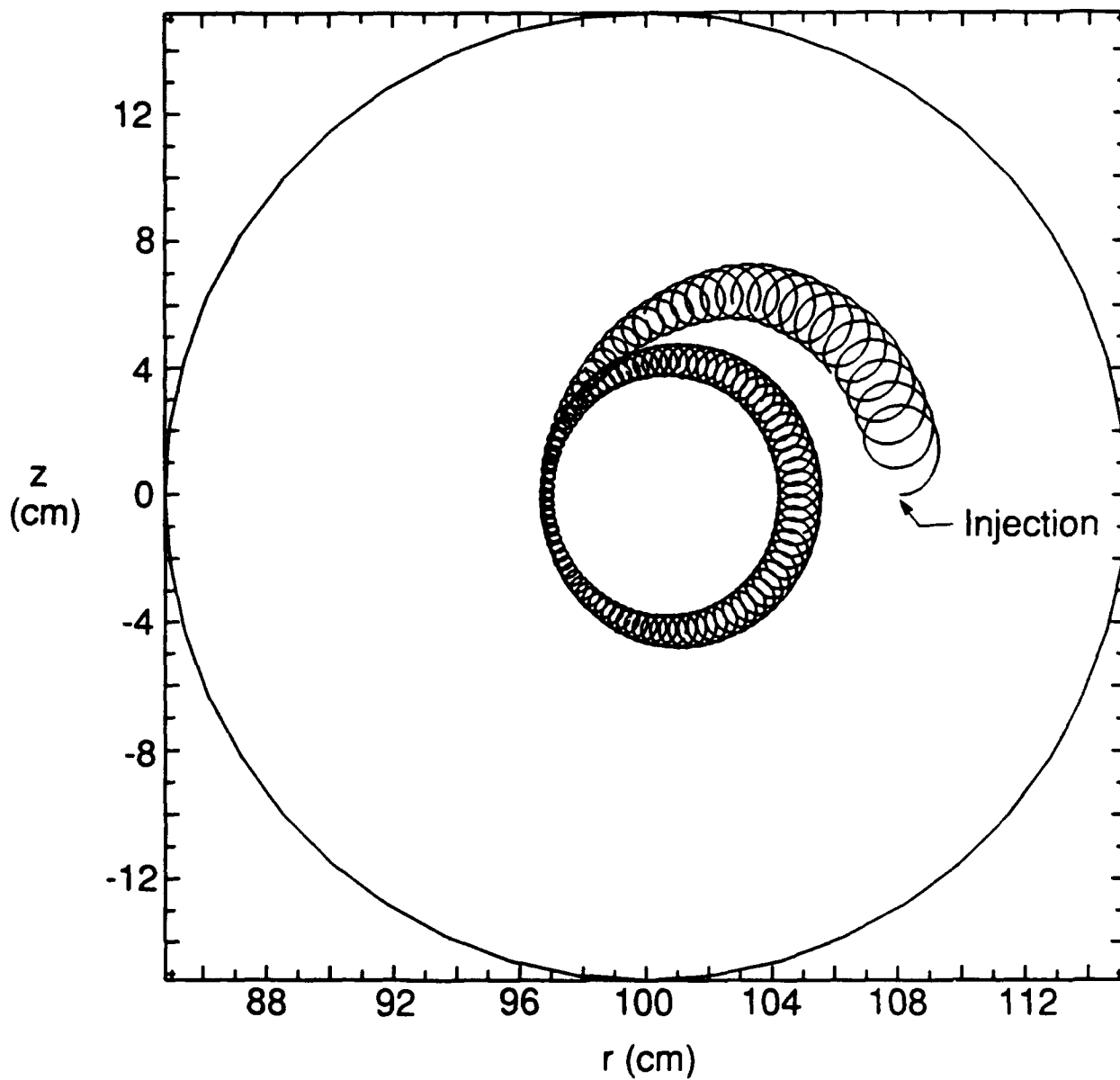


FIG. 9. Beam trapping for a 60-kV pulse.

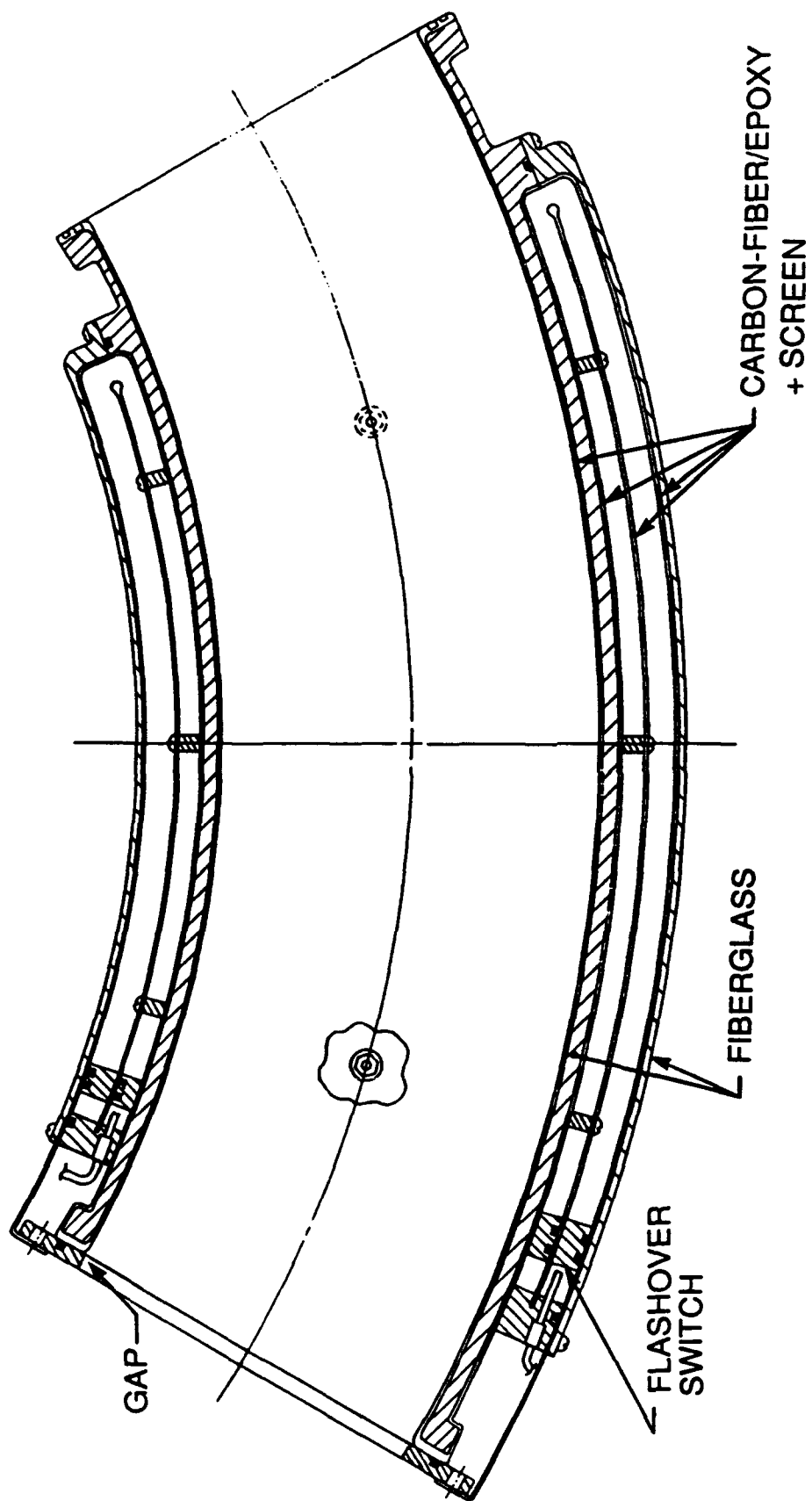


FIG. 10. Cross sectional view of the toroidal coaxial pulseline.

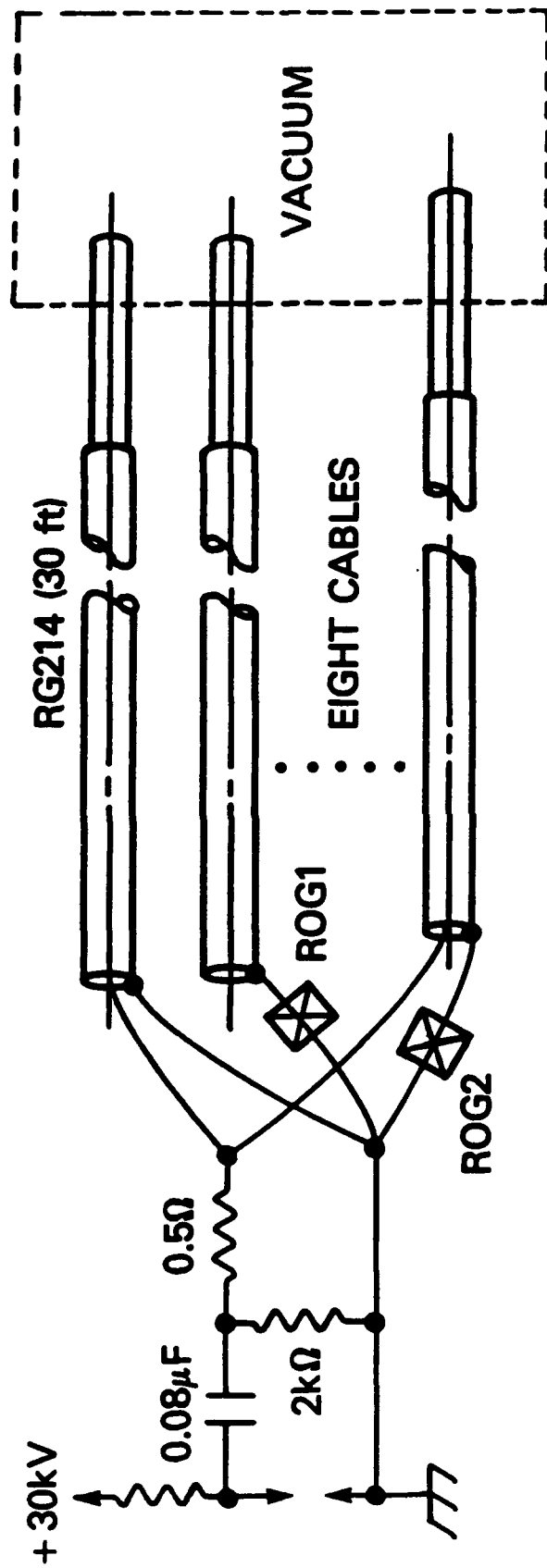


FIG. 11. Simplified circuit diagram of the initiation driver circuit used to trigger eight surface flashover sites in the pulseline.

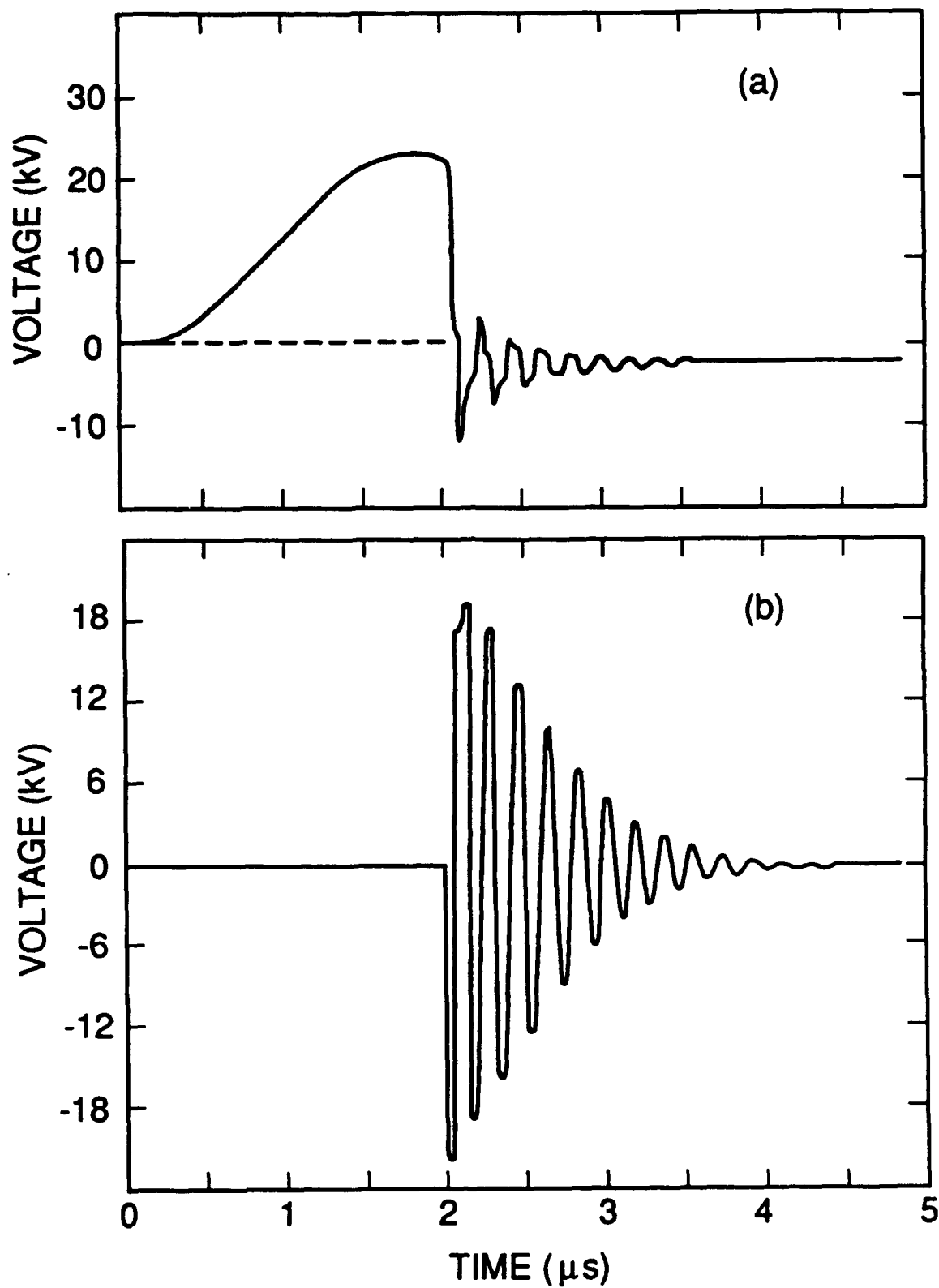


FIG. 12. (a) Pulseline charge voltage measured by capacitive probe CAP1. (b) Gap voltage waveform.

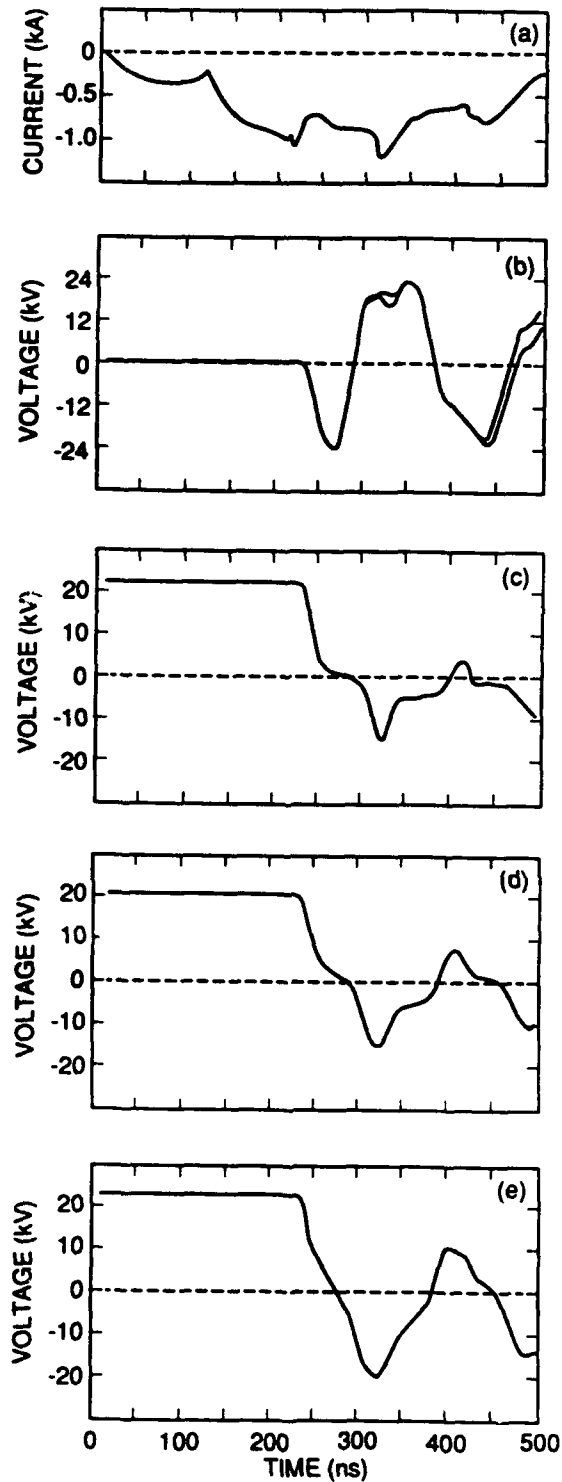


FIG. 13. Noncrowbarred pulseline waveforms for 22-kV charge voltage. (a) Trigger coax current, (b) gap voltage waveform (two shot overlay), (c) voltage measured by capacitive probe CAP1 in water, (d) voltage measured by CAP3 and (e) voltage measured by CAP4.

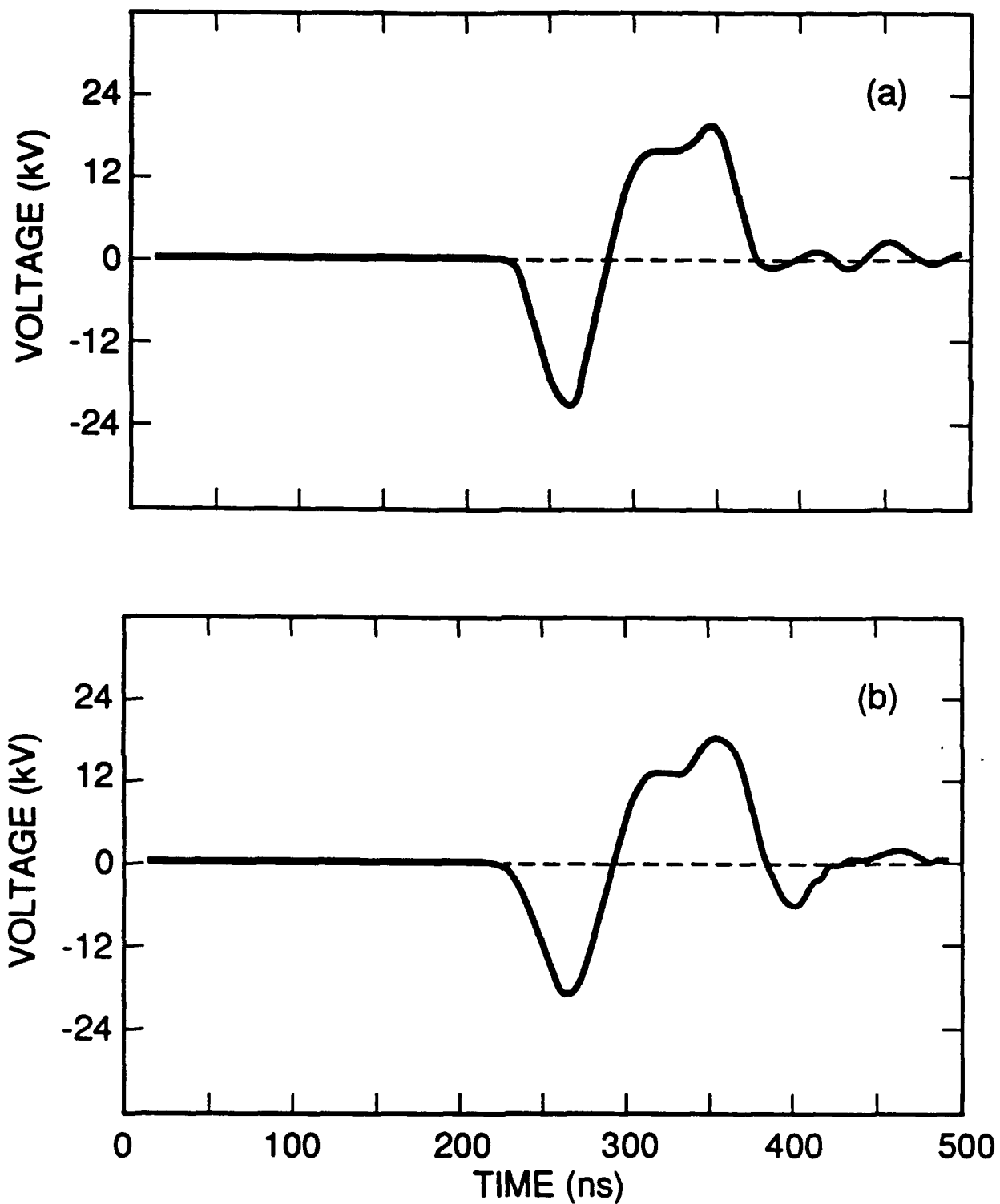
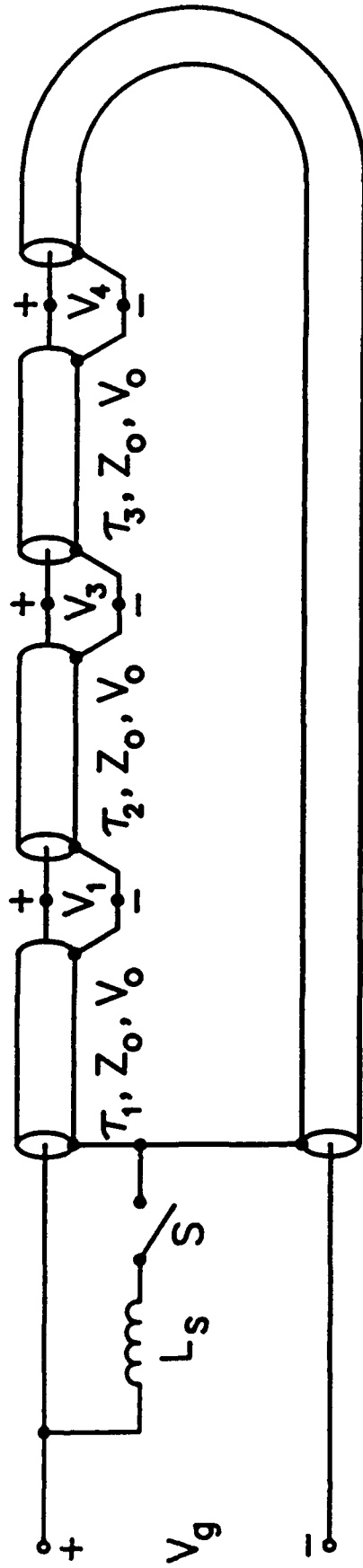


FIG. 14. Crowbarred gap voltage waveforms for 22-kV charge voltage. The crowbar switches fire 20 ns later for (b).



$$\tau_4, Z_0, V_0$$

FIG. 15. Transmission line representation of the toroidal pulse line for 1-D simulations.

$$\tau_1 = 6.0 \text{ ns}, \tau_2 = 6.3 \text{ ns}, \tau_3 = 6.3 \text{ ns}, \tau_4 = 26.4 \text{ ns}, \sum_{i=1}^4 \tau_i = \tau = 45 \text{ ns}, Z_0 = 0.84$$

Ω , $V_0 = 25 \text{ kV}$ and $L_s = 8 \text{ nH}$. V_g represents the gap voltage. V_1 , V_3 and V_4 represent the voltages measured by probes CAP1, CAP3 and CAP4. The switch

S closes at $\tau = 0$.

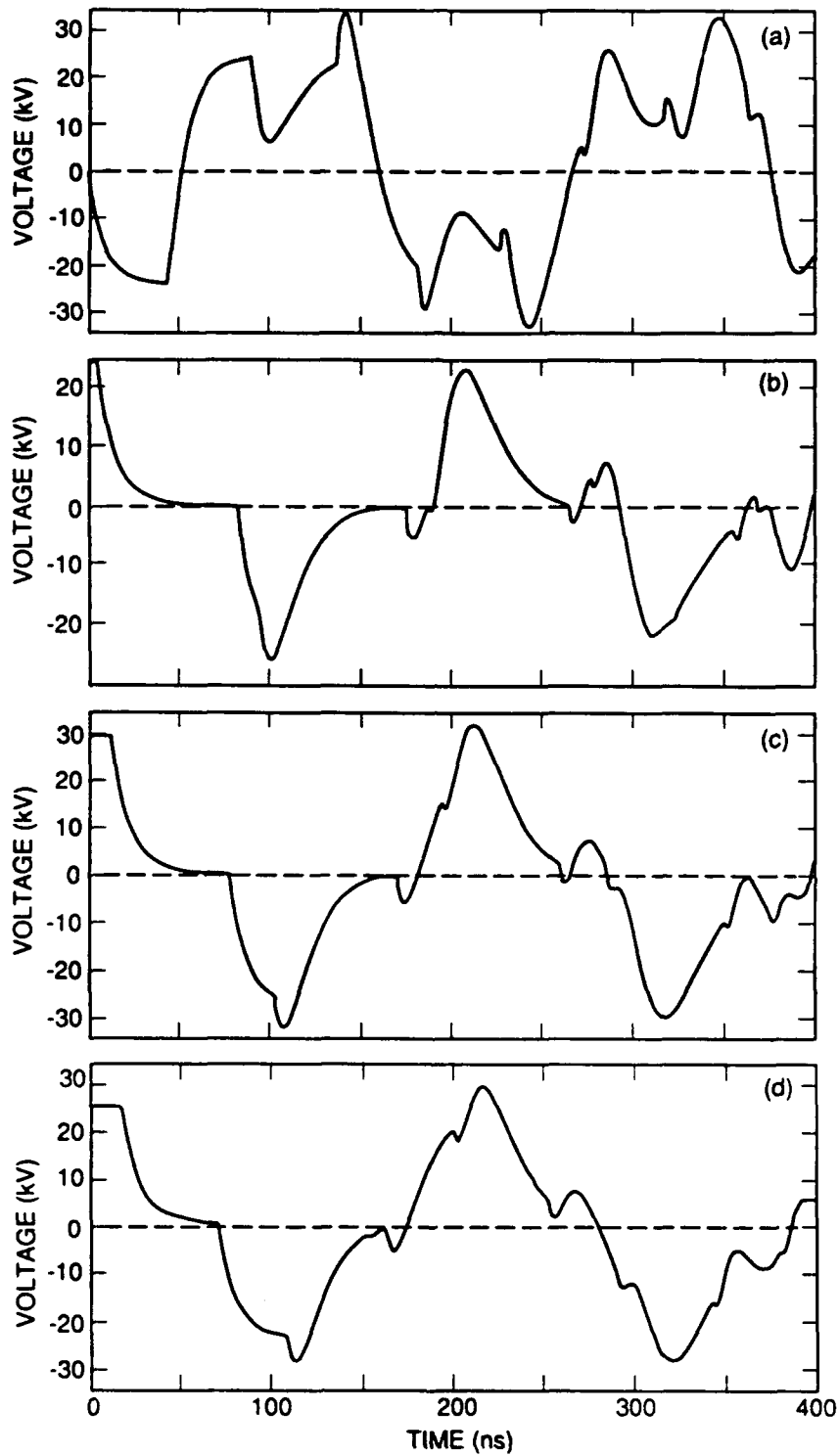


FIG. 16. (a) Simulated gap voltage waveform using the 1-D transmission line code. (b) thru (d) show the simulated waveforms corresponding to the voltages measured by CAP1, CAP3, and CAP4.